Study of the reaction $p_{\uparrow}p \to p\pi^+n$ with polarized beam from 3 to 12 GeV/c

A. B. Wicklund, M. W. Arenton,* D. S. Ayres, R. Diebold, S. L. Kramer, E. N. May, L. J. Nodulman, and J. R. Sauer†

Argonne National Laboratory, Argonne, Illinois 60439

(Received 16 December 1985)

We present density-matrix elements and single-spin correlations for the reaction $p_{\uparrow}p \to p\pi^+n$ at 3, 4, 6, and 11.75 GeV/c, using both longitudinal and transverse beam polarizations. For small momentum transfers, the spin correlations are mainly due to off-shell π^+p elastic scattering, while for larger t there are large polarization effects associated with the production dynamics for $p_{\uparrow}p \to \Delta^{++}n$. Comparison of longitudinal and transverse polarization correlations suggests that the Δ^{++}-production spin effects are due mainly to unnatural-parity exchanges. We present a model-dependent amplitude analysis, and extract the energy dependence of the natural- and unnatural-parity-exchange contributions.

I. INTRODUCTION

We present measurements of single-spin correlations and density-matrix elements in the reaction

$$p_{\uparrow}p \to p\pi^+n \ , \tag{1}$$

at 3, 4, 6, and 11.75 GeV/c, based on samples of 495 000, 550 000, 1 072 000, and 2 047 000 events, respectively. The data were taken with the effective-mass spectrometer (EMS), using the polarized proton beam from the Zero Gradient Synchrotron (ZGS). Both longitudinal- and transverse-polarization data were obtained at the higher energies, 6 and 11.75 GeV/c; comparison of these different polarization states permits model-independent separation of natural- and unnatural-parity-exchange contributions. Some preliminary results based on the lower-energy transverse-polarization data have been reported elsewhere.[1]

The quasi-two-body reaction

$$pp \to \Delta^{++}(1236)n \tag{2}$$

has been studied from threshold to CERN ISR energies,[2] with unpolarized beams and with lower statistics than the EMS experiment. The only data on spin correlations above 1.5 GeV/c are those from the EMS experiment and from the 6-GeV/c bubble-chamber exposure reported by Eisner *et al.*[3] Note that, owing to the Pauli principle, the spin-averaged cross sections for reactions (1) and (2) are symmetric for forward and backward scattering. However, the spin correlations need not be symmetric, and involve different physics for the two domains: small momentum transfer from the polarized beam to the outgoing neutron, as studied by Eisner *et al.*,[3] and from the polarized beam to the Δ^{++}, which is the case for the EMS experiment. To the extent that pion exchange dominates at these energies, the spin correlations involving the proton-neutron vertex are sensitive to π-A_1 interference, while those involving the proton-Δ^{++} vertex (e.g., as in the EMS experiment) require π-B interference. We remark that π-A_1 interference has been studied in the analogous charge-exchange (CEX) reaction[4]

$$\pi^-p_{\uparrow} \to \rho^0(770)n \ . \tag{3}$$

Large polarization effects are seen in reaction (3) and in both kinematical regions for reaction (2).

We present elsewhere[5] our analysis of EMS data on reaction (1) for momenta from 1.2 to 2.0 GeV/c. The combined results from the EMS experiments allow a detailed examination of the development of reaction (2) from threshold to high energy. This is of particular interest in the study of dibaryon resonances, since it has become clear that these phenomena are either threshold effects in the pp-$N\Delta$ coupled channels, or Breit-Wigner resonances, and in the latter case, they must decay predominantly into the $N\Delta$ channels. The higher-energy data reported here may be regarded as the "nonresonant" background against which the low-energy structures should be compared. It turns out that there are significant energy dependences in the spin correlations, particularly in the "resonance" region.

Our goal in this paper is to present the experimental measurements and the formalism needed to relate amplitudes and observables. In order to differentiate "trivial" sources of spin dependence, namely, off-shell pion-proton elastic scattering in reaction (1), from those involving the production dynamics of reaction (2), we have compared our data with a simple pion-exchange model, the Williams model (WM).[6,7] We have also examined the energy dependence of the natural- (NP) and unnatural-parity- (UP) exchange contributions, using quark-model arguments and the comparison of longitudinal- and transverse-polarization correlations; from these considerations we have been led to a model-dependent amplitude analysis of reaction (2).

The plan of the paper is as follows: Sec. II covers the experiment and the data analysis; Sec. III reviews the density-matrix element formalism we have adopted; Sec. IV presents the experimental observables; Sec. V reviews the NP-UP separation and the amplitude analysis; and Sec. VI concludes with a summary. The Appendix describes the pion-exchange parametrization.

II. EXPERIMENT AND DATA ANALYSIS

The topology of reaction (1), involving two forward charged tracks and a neutral recoil, is identical to that of other CEX reactions studied with the EMS (Refs. 7–9), and the trigger logic and event reconstruction details were essentially the same as described in Ref. 7. The beam line and the hydrogen-target station evolved considerably over the course of the experiment. For the earlier 3-, 4-, and 6-GeV/c transverse-polarization running, the beam was transported by a conventional magnet string to a 20-in. liquid-hydrogen target, as described in Ref. 10. The 11.75-GeV/c data taking required a superconducting beam line and used a thinner-walled 10-in. liquid-hydrogen target, as in Ref. 11. For the longitudinal-polarization measurements at 6 and 11.75 GeV/c the beam line was further modified by inclusion of two superconducting solenoids; the combination of solenoid and dipole magnetic fields was arranged to precess the proton spin from the vertical direction at the start of the beam line, to a direction parallel (antiparallel) to the proton momentum at the hydrogen target at 11.75 (6) GeV/c. In addition, the longitudinal data taking made use of a recoil-particle vertex detector which was intended for experiments on diffractive reactions; for reaction (1) the device was used only in software to improve background rejection. The EMS configuration used for this running, including the beam line and the vertex detector, was essentially as described in Ref. 12.

In brief, the event trigger used a hodoscope downstream of the EMS analyzing magnet, together with a hole-dE/dx counter upstream of the magnet, to impose a two-prong topology requirement; in addition, a neutral recoil requirement was imposed by a system of veto counters placed around the hydrogen target and the upstream aperture of the spectrometer magnet. Systematic corrections for hodoscope inefficiency and false vetoes due to δ rays and recoil-neutron interactions were measured with special runs having looser trigger conditions, as in Ref. 7.

Since the recoil neutron was not detected, the identification of reaction (1) depended on the missing-mass constraint provided by the forward momentum-analyzed tracks, e.g.,

$$pp \rightarrow p_f \pi_s^+(X) , \tag{3a}$$

$$pp \rightarrow p_s \pi_f^+(X) , \tag{3b}$$

where we have indicated the possible ambiguity in the identification of the forward fast and slow (f,s) tracks. At 3 and 4 GeV/c the resolution in $M_X{}^2$ was good enough to provide unambiguous identification of the final state, but for the higher energies, Cherenkov identification was essential. This was provided by a large aperture, segmented, high-pressure Cherenkov vessel placed downstream of the spectrometer. This device has been described in Ref. 13, and its use in other CEX reactions is discussed in Ref. 9. For reaction (1) the Cherenkov threshold was set at 1.45, 1.56, 2.0, and 3.0 GeV/c pion momentum, respectively, at 3, 4, 6, and 11.75 GeV/c beam momentum. Figure 1 provides an example of the use of this counter; we have selected samples of events in which the counter did not fire, which is the most common topology for reaction (1) and, even more so, for reaction (2). Figures 1(a), 1(c), and 1(e) show the $M_X{}^2$ distributions for the correct final-state hypothesis, namely, reaction (3a) (fast proton, slow pion), while Figs. 1(b), 1(d), and 1(f) show $M_X{}^2$ for the incorrect hypothesis (slow proton, fast pion). It is clear that (3a) and (3b) cannot be separated by $M_X{}^2$ alone on an event-by-event basis for 6 and 11.75 GeV/c, but the level of misidentification can be estimated statistically by comparing the $M_X{}^2$ distributions for the "correct" and "incorrect" hypotheses.

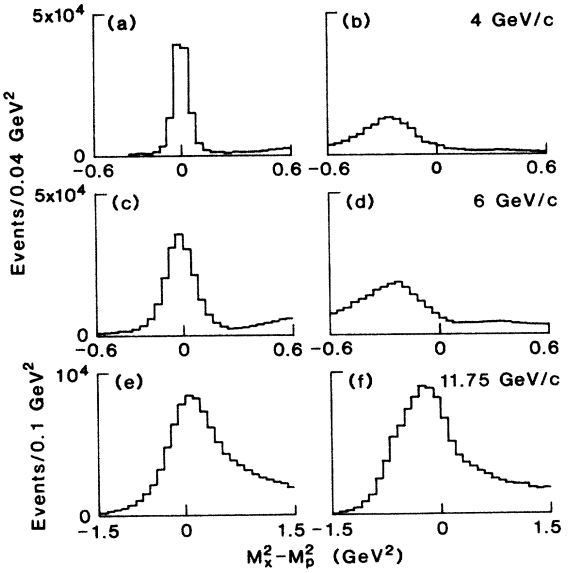

FIG. 1. Missing-mass-squared distributions for $pp \rightarrow p\pi^+(x)$ for 4, 6, and 11.75 GeV/c for events which did not fire the Cherenkov counter; (a), (c), and (e) are for the correct hypothesis, namely, fast proton and slow pion for the final-state charged tracks, while (b), (d), and (f) are for the incorrect hypothesis.

For ($p\pi^+$) masses above the Δ^{++} peak, the charged pion can be above Cherenkov threshold, and we have examined the appropriate missing-mass plots for events in which the counter did fire for a variety of topologies. Identification ambiguities occur at the $\sim$5% level, and for these events we chose hypothesis (3a). We used events from the reaction

$$pp \rightarrow p\pi^-(\Delta^{++}) \tag{4}$$

to calibrate the Cherenkov efficiency and the selection algorithms. Using a Monte Carlo simulation with a realistic $p\pi^+$ mass spectrum, we have estimated that Cherenkov-identification errors would result in a $\sim$1.5% loss of good events in the Δ^{++} band, and a $\sim$1.5% background from misidentified higher-mass events. No further corrections were made in the analysis for these small biases. After Cherenkov selection, missing-mass cuts on $M_X{}^2$-$M_p{}^2$ of $\pm$0.12, 0.16, 0.24, and 0.60 GeV^2 were imposed at 3, 4, 6, and 11.75 GeV/c, respectively. Events surviving these cuts were kinematically fitted to the recoil-neutron hypothesis.

In addition to two-prong triggers, the EMS recorded random beam triggers to help monitor the effective beam fluxes, and elastic scatters to monitor the beam polarization. The elastic scatters were also useful in maintaining the momentum calibration and alignment of the spectrometer, especially at the higher momenta where the $M_X{}^2$ resolution was poorest. The beam polarizations were obtained by fitting the raw asymmetries to polynomials in t, the shapes of which were fixed by elastic polarization data from other experiments.[14] The elastic asymmetries obtained in this fashion served to calibrate the CERN polarimeter[15] in the main extracted beam line. This in turn was used to determine the polarization for the longitudinal running. We obtained transverse polarizations of 80%, 72%, 63%, and 47%, respectively at 3, 4, 6, and 11.75 GeV/c, and longitudinal polarizations of 65% and 55% at 6 and 11.75 GeV/c; we ascribe an overall scale uncertainty of $\pm 10\%$ for these values, owing mainly to uncertainties in the elastic analyzing powers at these energies.

The beam spin was flipped on alternate ZGS pulses. The relative fluxes for spin up and down were found to be equal to better than 1%. Systematic uncertainties in these relative fluxes could in principle lead to false asymmetries; however, these false asymmetries are negligible compared with the statistical errors.

The fitted events from reaction (1) were binned in $M_{p\pi^+}$ and t (the momentum transfer from the polarized proton to the Δ^{++}). The events were then fitted to the most general moments expansion allowed by parity conservation:

$$p_{\rm lab}{}^2 \frac{d^4\sigma}{dt\, dM_{p\pi^+} d\Omega} = \sum_{L,M} [\, a_{LM}\, \mathrm{Re}Y_L^M(\theta,\phi) + P_x b_{LM}\, \mathrm{Im}Y_L^M(\theta,\phi) + P_y c_{LM}\, \mathrm{Re}Y_L^M(\theta,\phi) + P_z d_{LM}\, \mathrm{Im}Y_L^M(\theta,\phi)] \,, \tag{5}$$

where $\Omega=(\theta,\phi)$ gives the proton direction in the $p\pi^+$ rest frame (RF). The Cartesian components of the beam polarization vector refer to a system of axes in which $\hat{z}$ is parallel to the beam direction and $\hat{y}$ is along the overall production normal defined by $\mathbf{p}_{\rm beam}\times\mathbf{p}_\Delta$. The unpolarized coefficients a_{LM} were obtained by spin averaging the data; d_{LM} were obtained by comparison of spin-parallel and -antiparallel longitudinal data, and b_{LM} and c_{LM} by comparison of spin-up and -down transverse data, using the relations

$$P_x = P_\perp \sin\psi \,, \tag{6a}$$

$$P_y = P_\perp \cos\psi \,, \tag{6b}$$

where $P_\perp$ is the transverse polarization and ψ is an azimuthal angle defining the relative orientation of the spin vector and the production normal.

To correct for geometrical acceptance, we used the maximum-likelihood procedure described in Ref. 7. For each point in $M_{p\pi^+}$, t, θ, and ϕ phase space, the acceptance can be defined by an allowed range in the angle ψ:

$$\epsilon(M_{p\pi^+},t,\theta,\phi) = \frac{1}{2\pi}\int_{\rm allowed} d\psi \,. \tag{7}$$

The ψ range was defined analytically by fiducial cuts which were imposed on the events and on the acceptance calculation. Additional nongeometrical corrections, for example, those due to secondary interactions, varied slowly with ψ and were applied in essentially multiplicative fashion. The correctness of the procedure was checked by examining the ψ distributions and by varying the allowed ψ apertures.

The maximum-likelihood solution for the spin-averaged moments can be expressed by the coupled equations

$$\sum_i \frac{\mathrm{Re}Y_L^M(\theta_i,\phi_i)}{\sigma_0(\theta_i,\phi_i,a_{LM})} = F\int \frac{\epsilon(M,t,\Omega)\mathrm{Re}Y_L^M(\theta,\phi)\sum_{L',M'}\mathrm{Re}Y_{L'}^{M'}(\theta,\phi)a_{L'M'}\,dM\,dt\,d\Omega}{\sigma_0(\theta,\phi,\hat{a}_{LM})} \,, \tag{8}$$

where the sum on the left-hand side (LHS) is over events (i) in the bin, and F is the luminosity in events/mb. The quantity σ_0 denotes the unpolarized cross section,

$$\sigma_0(\theta,\phi,\hat{a}_{LM}) = \sum_{L,M}\hat{a}_{LM}\,\mathrm{Re}Y_L^M(\theta,\phi) \,, \tag{9}$$

and $\hat{a}_{LM}$ are any set of starting values that satisfy positivity and are reasonably close to the true solution, a_{LM}.

The polarization coefficients are obtained in analogous fashion, except that the sum over events on the LHS of Eq. (8) is replaced by the difference of sums over spin-up and -down events. For example, for the longitudinal case we have

$$\left[\sum_\uparrow - \sum_\downarrow\right]\frac{P_z\,\mathrm{Im}Y_L^M(\theta_i,\phi_i)}{\sigma_0(\theta_i,\phi_i,\hat{a}_{LM})} = FP_z^2\int \frac{\epsilon(M,t,\Omega)\,\mathrm{Im}Y_L^M(\theta,\phi)\sum_{L',M'}\mathrm{Im}Y_{L'}^{M'}(\theta,\phi)d_{L'M'}\,dM\,dt\,d\Omega}{\sigma_0(\theta,\phi,\hat{a}_{LM})} \,. \tag{10}$$

[Equation (10) assumes equal luminosities, $F_\uparrow = F_\downarrow$, for the up and down samples, with $F = F_\uparrow + F_\downarrow$.] The corresponding equations for b_{LM} and c_{LM} are coupled, and require explicit integration of $\sin^2\psi$, $\sin\psi\cos\psi$, and $\cos^2\psi$ over ψ on the RHS of Eq. (10), owing to relation (6).

Both Eqs. (8) and (10) give unbiased estimates for the moments and are good approximations to the exact maximum-likelihood prescription. The error matrices for the moments follow directly from Eqs. (8) and (10).

Systematic corrections were made for reconstruction

inefficiency [(5±4)%], trigger inefficiency [(2±2)%], secondary interactions in the target and spectrometer [$\sim$(6±3)% for the 10-in. target, depending on kinematical configuration], and vetoes caused by δ rays and secondary interactions [$\sim$(10±4)%]. We estimate a systematic uncertainty of ±10% on the overall normalization, in addition to the ±10% uncertainty in the values of the beam polarization.

The missing mass peaks in Fig. 1 indicate the presence of backgrounds from processes such as

$$pp \to p\pi^+(\Delta^0) \ . \tag{11}$$

To correct for these backgrounds, we binned the data in somewhat coarser bins in $M_{p\pi^+}$ and t, and carried out the moments fits as functions of $M_X{}^2$. The $M_X{}^2$ spectra for each moment were fitted to Gaussian signals plus polynomial backgrounds, including terms representing reaction (11). These backgrounds, and also the signal losses associated with the finite cutoffs on $M_X{}^2$, were interpolated in $M_{p\pi^+}$ and t and applied as corrections to the moments data base. It is difficult to attach a rigorous uncertainty to these background corrections; what we have done is to assign an error, equal to half the background correction, which we have added in quadrature to the statistical errors on the moments.

III. FORMALISM

Before examining the data, we summarize the formalism which we have developed for reaction (1). First, we use the Basel-convention production normal given by

$$\mathbf{y} = \mathbf{p}_b \times \mathbf{p}_\Delta \ , \tag{12}$$

where $\mathbf{p}_b$ and $\mathbf{p}_\Delta$ are the polarized beam proton and Δ^{++} momentum vectors in the overall cm. The Δ^{++} decay angles are defined by

$$\cos\theta = \mathbf{p}_p \cdot \mathbf{z} \ , \tag{13a}$$

$$\sin\theta\cos\phi = \mathbf{p}_p \cdot (\mathbf{y}\times\mathbf{z}) \ , \tag{13b}$$

$$\sin\theta\sin\phi = \mathbf{p}_p \cdot \mathbf{y} \ , \tag{13c}$$

where $\mathbf{p}_p$ is the proton momentum in the $p\pi^+$ (e.g., Δ^{++}) RF and z is the s- or t-channel z axis in that frame; we adhere to the usual conventions, namely,

$$\mathbf{z}_s = -\mathbf{p}_n \ , \tag{14a}$$

$$\mathbf{z}_t = +\mathbf{p}_b \ , \tag{14b}$$

where $\mathbf{p}_n$ and $\mathbf{p}_b$ are the recoil-neutron and beam-proton momenta in the $p\pi^+$ (RF).

We defined the s-channel Cartesian components of the beam polarization in Sec. II, namely, P_y is measured along $\mathbf{y}$, and P_z along the beam momentum direction. For t-channel observables, P_y is still measured along $\mathbf{y}$, but P_z is referred to the z axis given by the vector $-\hat{\mathbf{p}}_\Delta$ in the beam-proton RF. The s- and t-channel polarization components are related by a rotation around $\mathbf{y}$ given by

$$\begin{pmatrix} P_x \\ P_z \end{pmatrix}_{t\text{ channel}} = \begin{pmatrix} \cos\chi_p & \sin\chi_p \\ -\sin\chi_p & \cos\chi_p \end{pmatrix} \begin{pmatrix} P_x \\ P_z \end{pmatrix}_{s\text{ channel}} . \tag{15}$$

With the above z-axis conventions, $\chi_p \to 0$ for $t \approx t_{\min}$ and $\chi_p \approx 45°$ for larger t values. An analogous crossing angle χ_Δ relates the vectors $\mathbf{z}_s$ and $\mathbf{z}_t$ in Eq. (14) in the Δ^{++} RF; $\chi_\Delta \to 0$ for $t \approx t_{\min}$, and $\chi_\Delta \approx 90°$ for larger t values.

The Y_L^M moments in Eq. (5) with $L \geq 3$ turn out to be small in the fits for $M_{p\pi^+} < 1.4$ GeV, and we ignore them in the subsequent discussion. We can then recast the $L \leq 2$ moments in terms of 18 density-matrix elements (DME's):

$$\begin{aligned} p_{\text{lab}}{}^2 \frac{d^4\sigma}{dM_{p\pi^+} dt\, d\Omega} = \sigma_0 \frac{1}{4\pi} [\ & (\rho_{11}+P_y\rho_{11})(3\cos^2\theta+1)+(\rho_{33}+P_y\rho_{33})(3\sin^2\theta)-(\rho_{31}+P_y\rho_{31})(4\sqrt{3}\sin\theta\cos\theta\cos\phi) \\ & -(P_x\rho_{31}+P_z\rho_{31})(4\sqrt{3}\sin\theta\cos\theta\sin\phi)-(\rho_{3-1}+P_y\rho_{3-1})(2\sqrt{3}\sin^2\theta\cos2\phi) \\ & -(P_x\rho_{3-1}+P_z\rho_{3-1})(2\sqrt{3}\sin^2\theta\sin2\phi)+(\rho_{s1}+P_y\rho_{s1})(4\cos\theta) \\ & +(\rho_{s-1}+P_y\rho_{s-1})(4\sin\theta\cos\phi)+(P_x\rho_{s-1}+P_z\rho_{s-1})(4\sin\theta\sin\phi)] \ . \end{aligned} \tag{16}$$

For mnemonic purposes, we have specified the spin-averaged DME's by ρ_{ij}, and the spin correlations by $P_k\rho_{ij}$, where the latter are linear combinations of the b_{LM}, c_{LM}, and d_{LM} coefficients in Eq. (5). To avoid confusion, note that $P_k\rho_{ij}$ is a symbol and denotes the spin correlation for, e.g., 100% beam polarization along axis k.

Equation (16) provides a complete description for production of $p\pi^+$ isobars with internal orbital momenta, $l=0$ or 1. We will denote the $jP = \frac{1}{2}^-$, $\frac{1}{2}^+$, and $\frac{3}{2}^+$ waves, respectively, by s, p, and Δ; s and p are nonresonant background waves under the Δ^{++}, and are presumably related to the same waves in elastic π^+p scattering. Figure 2 depicts the probable origin of the three isobar contributions; all waves should be excited by pion exchange (2a), while Δ^{++} production may be mediated by other CEX mechanisms (2b). Because the Δ^{++}-production waves are clearly dominant, for discussion purposes we need consider only interferences of the type Δ-Δ, s-Δ, or p-Δ. Then the correlations involving ρ_{s1} and ρ_{s-1} in Eq. (16) arise from s-Δ interferences, while the other DME's are due to p-Δ or Δ-Δ contributions. The s- and p-wave amplitudes are a distinct nuisance; since the

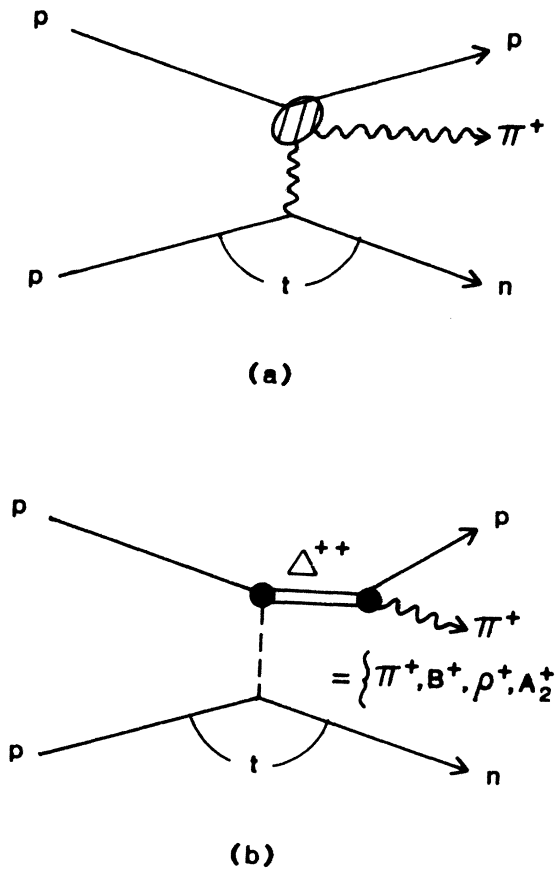

FIG. 2. Charge exchange mechanisms: (a) pion exchange with off-shell $\pi^+ p_\uparrow$ elastic scattering, and (b) Δ^{++} production by Regge exchanges.

Δ^{++} Breit-Wigner phase is $\sim 90°$ ahead of the s- and p-wave phase shifts in $\pi^+ p$ elastic scattering, $\mathrm{Im}(s^*\Delta)$ and $\mathrm{Im}(p^*\Delta)$ are nearly maximal and give rise to significant spin correlations. In order to expose the Δ-Δ interference terms, we need to remove the p-Δ interference contributions using, for example, a pion-exchange model. Fortunately, such a computation can be calibrated by the s-Δ interferences, which have the virtue of being isolated in the ρ_{s1}, ρ_{s-1} DME's.

To proceed further, we can expand the DME's in terms of s- or t-channel helicity amplitudes, e.g., $A^{\lambda_\Delta \lambda_b}_{\lambda_n \lambda_t}(M_{p\pi^+}, t)$, where λ_Δ, λ_b, λ_n, and λ_t are the helicities of the Δ^{++}, beam proton, recoil neutron, and target proton, respectively. It is convenient to work with linear combinations of the A's which correspond asymptotically to NP and UP exchanges, namely,

$$N^{\lambda_\Delta \lambda_b}_{++} = A^{\lambda_\Delta \lambda_b}_{++} + A^{\lambda_\Delta \lambda_b}_{--} , \tag{17a}$$

$$N^{\lambda_\Delta \lambda_b}_{-+} = A^{\lambda_\Delta \lambda_b}_{-+} - A^{\lambda_\Delta \lambda_b}_{+-} , \tag{17b}$$

$$U^{\lambda_\Delta \lambda_b}_{++} = A^{\lambda_\Delta \lambda_b}_{++} - A^{\lambda_\Delta \lambda_b}_{--} , \tag{17c}$$

$$U^{\lambda_\Delta \lambda_b}_{-+} = A^{\lambda_\Delta \lambda_b}_{-+} + A^{\lambda_\Delta \lambda_b}_{+-} , \tag{17d}$$

where $++$ denotes $(\lambda_n, \lambda_t) = (\frac{1}{2}, \frac{1}{2})$, etc. At the recoil-neutron target-proton vertex, the N amplitudes involve transitions of the form $1 + \sigma \cdot \hat{\mathbf{y}}$, whereas the U amplitudes are of the form $\sigma \cdot \hat{\mathbf{x}} + \sigma \cdot \hat{\mathbf{z}}$, where $\hat{\mathbf{x}}$ and $\hat{\mathbf{z}}$ are vectors in the scattering plane. Note that Eq. (17) applies to s and p, as well as Δ production. Because our experiment averages over target and recoil spins, there are no interferences between any of the four types of amplitudes in Eq. (17). Furthermore, because of parity conservation,

$$A^{-\lambda_\Delta - \lambda_b}_{-\lambda_n - \lambda_t} = (-1)^{\Sigma + \lambda_\Delta + \lambda_b - \lambda_n - \lambda_t} \eta A^{\lambda_\Delta \lambda_b}_{\lambda_n \lambda_t} , \tag{18}$$

only half of the amplitudes are independent, and we can fix $\lambda_b = +\frac{1}{2}$. [In Eq. (18), $\Sigma = \Sigma S_i = \frac{3}{2} + j$; j is the total J and $\eta = (-1)^{l+1}$ the intrinsic parity of the $p\pi^+$ system.] Thus, we drop $\lambda_b = \frac{1}{2}$ in Eq. (17), and refer henceforth to amplitudes N^M_{-+}, N^M_{++}, U^M_{-+}, and U^M_{++}, with $M = 2\lambda_\Delta$. We adopt a normalization such that

$$p_{\mathrm{lab}}{}^2 \frac{d^2\sigma}{dM_{p\pi^+} dt} = \sum_{j,l,M} \left[\frac{2j+1}{2} \right] \times (|U^M_{++}|^2 + |U^M_{-+}|^2 + |N^M_{++}|^2 + |N^M_{-+}|^2) . \tag{19}$$

The DME's all have the same formal expansion for each of the four N- and U-type amplitudes with one important exception: The transverse-polarization correlations $P_{x,y}\rho_{ij}$ have opposite signs for N^*N as for U^*U contributions, and so we introduce a naturality factor $\xi = +1$ (NP), -1 (UP) directly into the DME expansion. for brevity we use s^M, p^M, and Δ^M to denote production of s, p, or Δ waves by any of the U^M, N^M amplitudes; we can then express the Δ-Δ, s-Δ, and p-Δ contributions to the DME's as follows:

$$\sigma\rho_{11} = |\Delta^1|^2 + |\Delta^{-1}|^2 + \Delta^1 p^{1*} - \Delta^{-1} p^{-1*} , \tag{20a}$$

$$\sigma\rho_{33} = |\Delta^3|^2 + |\Delta^{-3}|^2 - \Delta^1 p^{1*} + \Delta^{-1} p^{-1*} , \tag{20b}$$

$$\sigma\rho_{31} = \Delta^1 \Delta^{3*} - \Delta^{-1}\Delta^{-3*} + \tfrac{1}{2}(\Delta^3 p^{1*} + \Delta^{-3} p^{-1*} - \sqrt{3}\Delta^1 p^{-1*} - \sqrt{3}\Delta^{-1} p^{1*}) , \tag{20c}$$

$$\sigma\rho_{3-1} = \Delta^1 \Delta^{-3*} + \Delta^{-1}\Delta^{3*} + \Delta^3 p^{-1*} - \Delta^{-3} p^{1*} , \tag{20d}$$

$$\sigma P_y \rho_{11} = \xi(-2\Delta^{-1}\Delta^{1*} - \Delta^{-1} p^{1*} - \Delta^1 p^{-1*}) , \tag{20e}$$

$$\sigma P_y \rho_{33} = \xi(2\Delta^{-3}\Delta^{3*} + \Delta^{-1} p^{1*} + \Delta^1 p^{-1*}) , \tag{20f}$$

$$\sigma P_y \rho_{31} = \xi[-\Delta^1\Delta^{-3*} - \Delta^{-1}\Delta^{3*} + \tfrac{1}{2}(\Delta^{-3} p^{1*} - \Delta^3 p^{-1*} + \sqrt{3}\Delta^{-1} p^{-1*} - \sqrt{3}\Delta^1 p^{1*})] , \tag{20g}$$

$$\sigma P_y \rho_{3-1} = \xi(-\Delta^{-1}\Delta^{-3*} + \Delta^1\Delta^{3*} + \Delta^{-3} p^{-1*} + \Delta^3 p^{1*}) , \tag{20h}$$

$$\sigma P_x \rho_{31} = \xi[-\Delta^1\Delta^{-3*} + \Delta^{-1}\Delta^{3*} + \tfrac{1}{2}(\Delta^{-3} p^{1*} + \Delta^3 p^{-1*} + \sqrt{3}\Delta^{-1} p^{-1*} + \sqrt{3}\Delta^1 p^{1*})] , \tag{20i}$$

$$\sigma P_x\rho_{3-1}=\xi(-\Delta^{-1}\Delta^{-3*}-\Delta^{1}\Delta^{3*}+\Delta^{-3}p^{-1*}-\Delta^{3}p^{1*}) , \tag{20j}$$

$$\sigma P_z\rho_{31}=\Delta^{-1}\Delta^{-3*}+\Delta^{1}\Delta^{3*} +\tfrac{1}{2}(-\Delta^{3}p^{1*}+\Delta^{-3}p^{-1*}+\sqrt{3}\Delta^{1}p^{-1*} -\sqrt{3}\Delta^{-1}p^{1*}) , \tag{20k}$$

$$\sigma P_z\rho_{3-1}=-\Delta^{1}\Delta^{-3*}+\Delta^{-1}\Delta^{3*}-\Delta^{-3}p^{1*}-\Delta^{3}p^{-1*} , \tag{20l}$$

$$\sigma\rho_{s1}=\Delta^{1}s^{1*}+\Delta^{-1}s^{-1*} , \tag{20m}$$

$$\sigma\rho_{s-1}=\tfrac{1}{2}(\Delta^{-1}s^{1*}-\Delta^{1}s^{-1*}+\sqrt{3}\Delta^{-3}s^{-1*}-\Delta^{3}s^{1*}) , \tag{20n}$$

$$\sigma P_y\rho_{s1}=\xi(-\Delta^{-1}s^{1*}+\Delta^{1}s^{-1*}) , \tag{20o}$$

$$\sigma P_y\rho_{s-1}=\xi[\tfrac{1}{2}(\Delta^{-1}s^{-1*}+\Delta^{1}s^{1*}-\sqrt{3}\Delta^{-3}s^{1*} -\sqrt{3}\Delta^{3}s^{-1*})] , \tag{20p}$$

$$\sigma P_x\rho_{s-1}=\xi[\tfrac{1}{2}(\Delta^{-1}s^{-1*}-\Delta^{1}s^{1*}-\sqrt{3}\Delta^{-3}s^{1*} +\sqrt{3}\Delta^{3}s^{-1*})] , \tag{20q}$$

$$\sigma P_z\rho_{s-1}=\tfrac{1}{2}(\Delta^{1}s^{-1*}+\Delta^{-1}s^{1*}+\sqrt{3}\Delta^{3}s^{1*} +\sqrt{3}\Delta^{-3}s^{-1*}) . \tag{20r}$$

Equation (20) is an implicit summation over the four noninterfering N_{-+}-, N_{++}-, U_{-+}-, and U_{++}-type amplitudes, and the amplitude products refer to Re(NN^*), Re(UU^*), for the unpolarized DME's, and Im(NN^*), Im(UU^*) for the polarization correlations.

There are several useful features to note regarding the amplitudes and observables.

(a) In the forward direction ($t=t_{\min}$, or $t'=0$), there are only four independent nonvanishing amplitudes having net helicity flip $n=0$; these are N^1_{++} and U^1_{++}, and the double-flip amplitudes, which are related by

$$N^3_{-+}(t'=0)=-U^3_{-+}(t'=0) , \tag{21a}$$

$$N^{-1}_{-+}(t'=0)=U^{-1}_{-+}(t'=0) . \tag{21b}$$

(b) The DME's which involve ϕ dependence in Eq. (16) should, naively, vanish at $t=t_{\min}$, where the production normal and, hence, also ϕ are undefined. The actual situation is more complicated, and we have the constraints

$$P_y\rho_{31}(t'=0)=-P_x\rho_{31}(t'=0) , \tag{22a}$$

$$P_y\rho_{s-1}(t'=0)=-P_x\rho_{s-1}(t'=0) . \tag{22b}$$

From Eq. (21) it is easy to show that all other ϕ-dependent DME's do vanish at $t=t_{\min}$. The nonvanishing terms in Eq. (22) survive because the correlation between the beam spin and the decay plane defined by the $p\pi^+$ system need not vanish at $t=t_{\min}$; this kind of correlation is expected for the off-shell π^+p elastic-scattering contribution of Fig. 2(a).

(c) The sums $2\sigma(\rho_{11}+\rho_{33})=\sigma$ and $2(P_y\rho_{11}+P_y\rho_{33})$ eliminate p-Δ interferences; the latter is analogous to the left-right asymmetry in any two-body scattering process, and the summation simply integrates over the $p\pi^+$ decay distribution.

(d) The Δ-Δ interferences in the P_x and P_z correlations are related [cf. Eqs. (20i)—(20l)]. For pure *UP* production ($\xi=-1$), we would have

$$P_x\rho_{31}=-P_z\rho_{3-1} , \tag{23a}$$

$$P_x\rho_{3-1}=P_z\rho_{31} , \tag{23b}$$

with opposite signs for pure *NP* production. This permits some separation of the different naturality contributions.

As noted above, in order to separate the s-Δ and p-Δ interference contributions from the Δ-Δ terms of interest, we have used a variant of the Williams model,[6] which essentially adds simple absorptive corrections to the Chew-Low[16] description for pion exchange; our parametrization has been shown to provide a fair description of analogous CEX processes such as ρ^0 production in reaction (3) (Ref. 7). Details are provided in the Appendix. The description involves seven free parameters at each energy; the parameter values, based on fits to the DME's ρ_{11}, ρ_{33}, ρ_{31}, and ρ_{3-1} over the interval $-t<0.6$ GeV^2, are listed in Table I. Physically the parametrization incorporates four key features: (1) the U^1 amplitudes dominate for small t', (2) the t-channel U^{-3} and N^{-3} amplitudes vanish, (3) the *NP* and *UP* flip amplitudes of Eq. (21) are nonzero for $t'=0$, and (4) s-channel U^3_{-+} and U^{-1}_{-+} have crossover zeros near $-t'=m_\pi{}^2$.

IV. RESULTS

This section provides a cursory review of the measured observables as functions of $M_{p\pi^+}$, t, and $p_{\rm lab}$. Data tables for all the s- and t-channel observables are available on request in a separate report.[17]

Figure 3 shows the differential cross sections for the

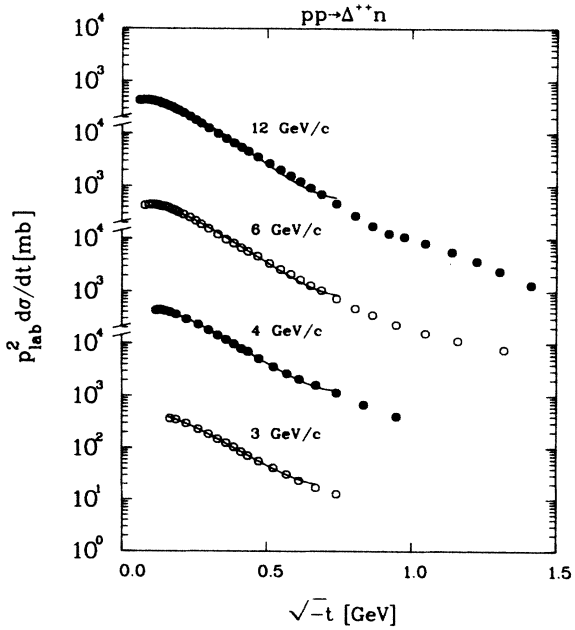

FIG. 3. Forward differential cross sections for $pp\to\Delta^{++}n$, with pion-exchange (WM) fits (solid curves); the cross sections have been corrected by a factor 1.24 to account for the Δ^{++} tail outside the selection band ($1.15<M_{p\pi^+}<1.34$ GeV).

TABLE I. The values of the seven parameters obtained from fits to the WM parametrization, over the range $-t < 0.6$ GeV^2. Also listed are the crossing factors $\tilde{P}_{-}^{M1}$ defined in the Appendix; these have been evaluated at $M_{p\pi^+} = 1.24$ GeV (except for $\tilde{P}_{-}^{11} = 1.00$, they have significant $M_{p\pi^+}$ dependence.) The errors are statistical only, and (f) denotes a fixed parameter.

	3 GeV/c	4 GeV/c	6 GeV/c	11.75 GeV/c
G (mb$^{1/2}$)	2.74(0.03)	3.07(0.02)	3.04(0.02)	3.21(0.03)
B (GeV^{-2})	1.54(0.08)	1.74(0.04)	2.29(0.03)	3.80(0.08)
B_- (GeV^{-2})	6.29(0.10)	7.09(0.12)	6.71(0.14)	6.83(0.28)
D_- (GeV^{-4})	6.20(f)	6.23(0.45)	5.35(0.10)	5.17(0.64)
B_+ (GeV^{-2})	6.75(0.08)	7.34(0.13)	6.60(0.33)	5.57(0.16)
D_+ (GeV^{-4})	9.00(f)	9.06(0.26)	7.16(0.19)	5.28(0.30)
S	1.27(0.02)	1.12(0.01)	1.07(0.01)	0.97(0.01)
$\tilde{P}_{-}^{31}(\Delta)$	2.69	2.41	2.15	1.91
$\tilde{P}_{-}^{11}(\Delta)$	−2.81	−2.73	−2.65	−2.57
$\tilde{P}_{-}^{11}(\Delta)$	1.00	1.00	1.00	1.00
$\tilde{P}_{-}^{31}(\Delta)$	3.57	3.56	3.55	3.50
$\tilde{P}_{-}^{11}(s)$	−0.76	−0.68	−0.61	−0.55
$\tilde{P}_{-}^{11}(s)$	1.00	1.00	1.00	1.00
$\tilde{P}_{-}^{11}(p)$	−3.36	−3.44	−3.49	−3.50
$\tilde{P}_{-}^{11}(p)$	1.00	1.00	1.00	1.00

Δ^{++} band ($1.15 < M_{p\pi^+} < 1.34$ GeV), corrected by a factor of 1.24 to account for the Δ Breit-Wigner tail outside of this band. The curves illustrate the fits to the WM parametrization. Figure 4 shows the mass spectra for $-t < 0.2$ GeV^2, together with the fits; the mass dependence is fixed by the $\pi^+ p$ elastic phase shifts [cf. Eq. (A1)], and adjusting the Δ Breit-Wigner parameters could clearly improve the fits somewhat. The mass spectra have essentially the same shape at larger t values as well. The integrated asymmetry $2(P_y\rho_{11} + P_y\rho_{33})$ is shown in Fig. 5. The solid curves are simply a polynomial interpolation chosen to be identical at all four energies, so as to display better the $p_{\rm lab}$ dependence. This asymmetry would vanish for the WM, and must be due to $\Delta^*\Delta$ interference terms associated with π, B, ρ, and A_2 exchanges; note that A_1 exchange, although prominent in reaction (3), should not contribute strongly to this asymmetry, because π-A_1 interference vanishes in averaging over target and recoil helicities.

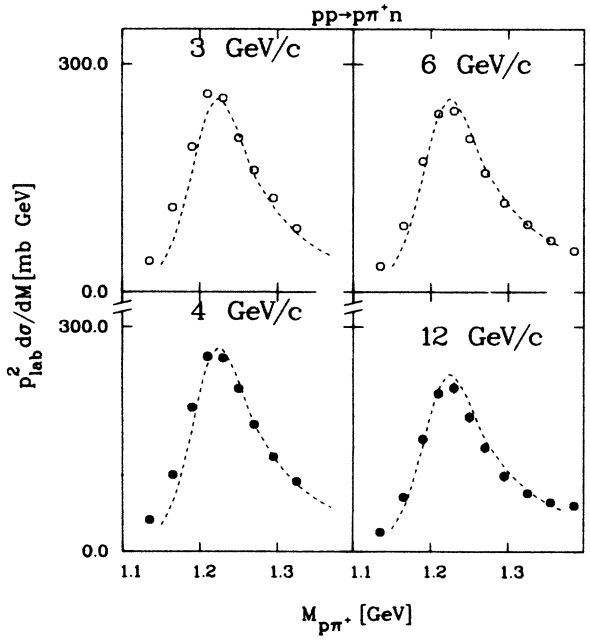

FIG. 4. Mass distributions with WM predictions for $-t < 0.2$ GeV^2.

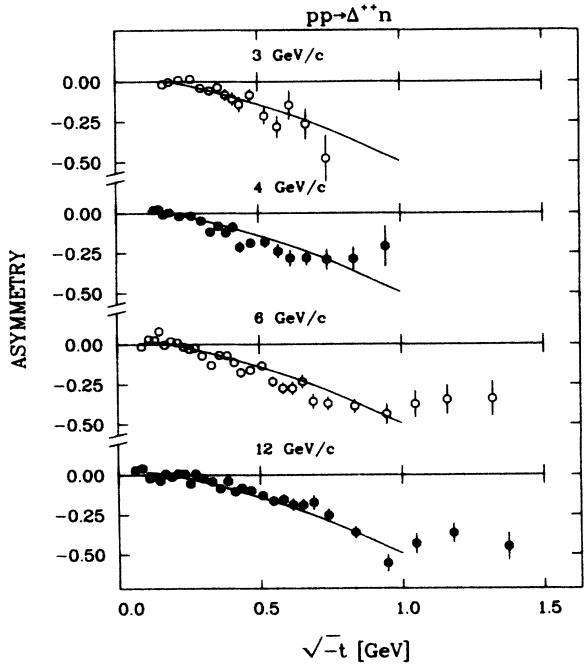

FIG. 5. Integrated left-right asymmetry, $2(P_y\rho_{11} + P_y\rho_{33})$ for the Δ^{++} band (1.15–1.34 GeV). The solid curves are a fixed polynomial obtained from an average of the 6- and 11.75-GeV/c data.

The unpolarized DME's, ρ_{11}, ρ_{33}, ρ_{31}, ρ_{3-1}, ρ_{s1}, and ρ_{s-1} are shown in the s channel in Figs. 6(a)–6(f), respectively, and in the t channel in Figs. 7(a)–7(f), together with the WM fits. Some of the characteristic features of the WM model, which follow from the absorptive cuts in the $n=0$ double-flip amplitudes, are (1) a sharp forward peak in s-channel ρ_{33} [Fig. 6(b)], and (2) crossover zeros near $-t=m_\pi{}^2$ for s-channel ρ_{31} and ρ_{s-1} [Figs. 6(c) and 6(f)]. In the t channel, the DME's are slowly varying at small t, similar to other t-channel pion-exchange reactions such as ρ^0 production [reaction (3)] and also

$$K^+n\to K^{*0}(890)p\ , \tag{24a}$$

$$K^-p\to \bar{K}^{*0}(890)n\ . \tag{24b}$$

Note that $\rho_{3-1}\approx 0$ in the t channel [Fig. 7(d)], as expected in the WM; this is analogous to $\rho_{1-1}\approx 0$ for the ρ^0 and K^{*0} production reactions. In Figs. 6(e) and 6(f), and 7(e)

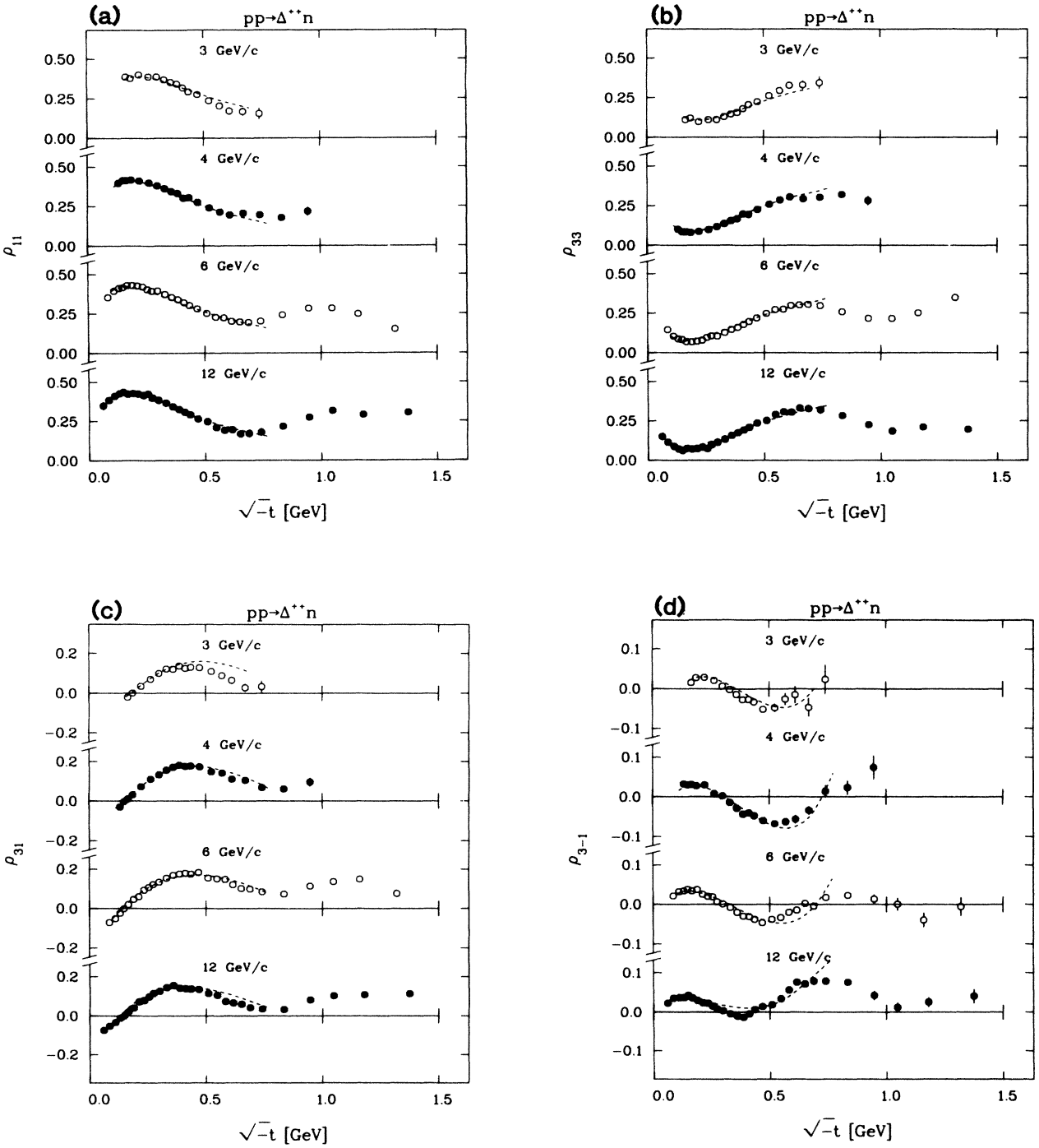

FIG. 6. (a) s-channel ρ_{11} in the Δ^{++} band (1.15–1.34 GeV), with the WM fits (dashed curves), plotted against $\sqrt{-t}$. (b) s-channel ρ_{33}, as in (a). (c) s-channel ρ_{31}, as in (a). (d) s-channel ρ_{3-1}, as in (a). (e) s-channel ρ_{s1}, for the band $1.24<M_{p\pi^+}<1.34$ GeV, with WM predictions (dashed curves). (f) s-channel ρ_{s-1}, as in (e).

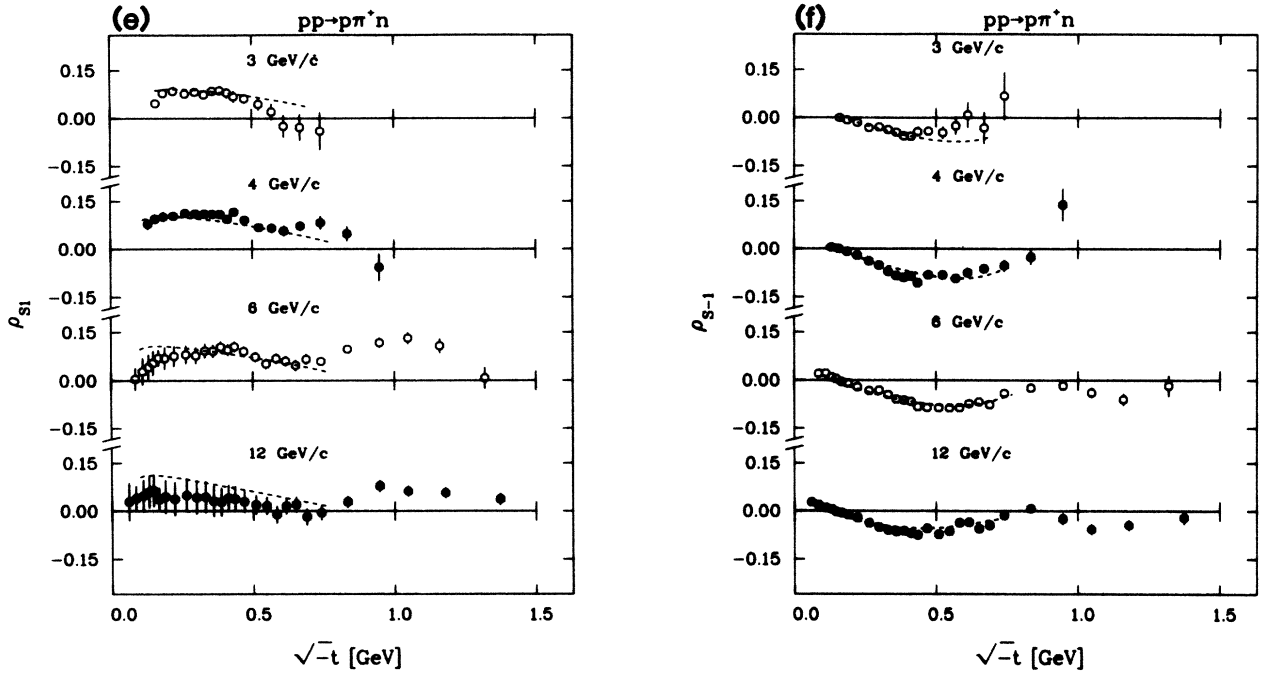

FIG. 6. (*Continued*).

and 7(f) we have shown ρ_{s1} and ρ_{s-1} for the high-mass side of the Δ^{++}, $1.24 < M_{p\pi^+} < 1.34$ GeV, whereas the other DME's are for the full Δ^{++} band ($1.15 < M_{p\pi^+} < 1.34$ GeV). This is because ρ_{s1} and ρ_{s-1} are proportional to $\mathrm{Re}(s^*\Delta)$ in the WM, and are expected to change sign near the Δ mass where $\delta_\Delta - \delta_s \simeq 90°$. The mass dependence of these DME's, for $-t < 0.2$ GeV^2, bears out these expectations (Fig. 8); the solid circles in Fig. 8 show ρ_{s-1}, the open circles ρ_{s1}. (The larger error bars on the 11.75-GeV/c data for ρ_{s1} simply reflect the larger background subtractions for this DME, as explained in Sec. II.) We remark that not only ρ_{s1} and ρ_{s-1}, but also the DME's which are dominated by Δ-Δ contributions, show appreciable mass dependence; this is qualitatively explained by the mass dependence of the crossing factors in the WM. For example, Fig. 9 shows the mass

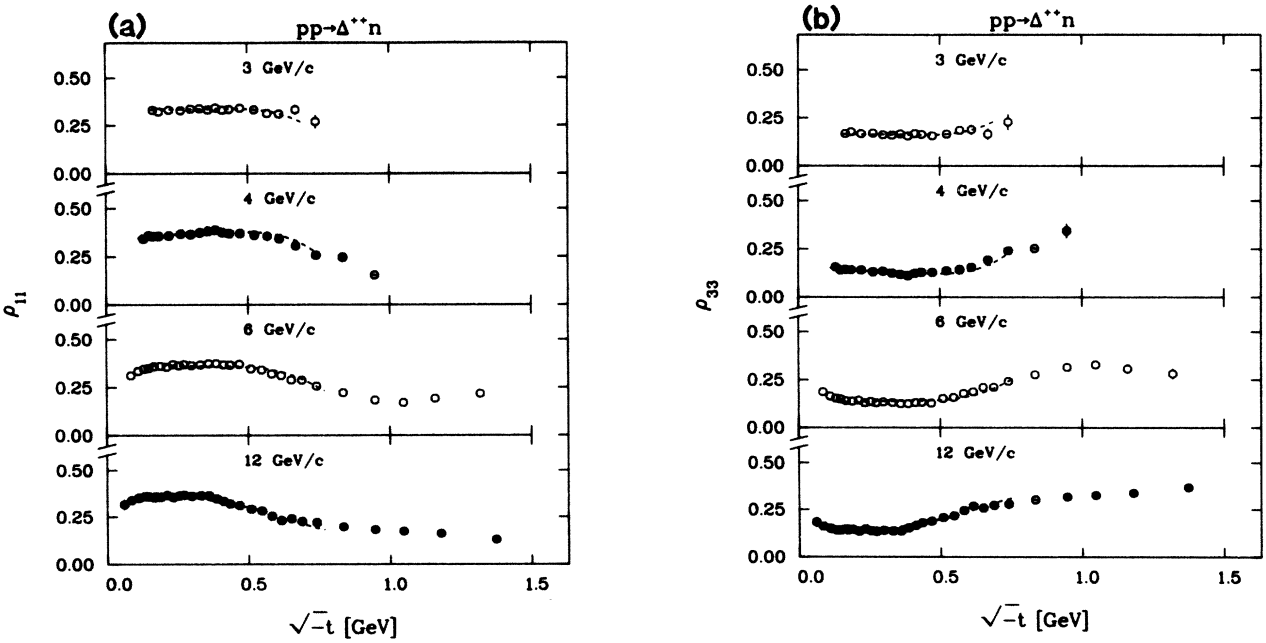

FIG. 7. (a) t-channel ρ_{11} in the Δ^{++} band (1.15—1.34 GeV), with the WM fits (dashed curves), plotted against $\sqrt{-t}$. (b) t-channel ρ_{33}, as in (a). (c) t-channel ρ_{31}, as in (a). (d) t-channel ρ_{3-1}, as in (a). (e) t-channel ρ_{s1}, for the band $1.24 < M_{p\pi^+} < 1.34$ GeV, with WM predictions (dashed curves). (f) t-channel ρ_{s-1}, as in (e).

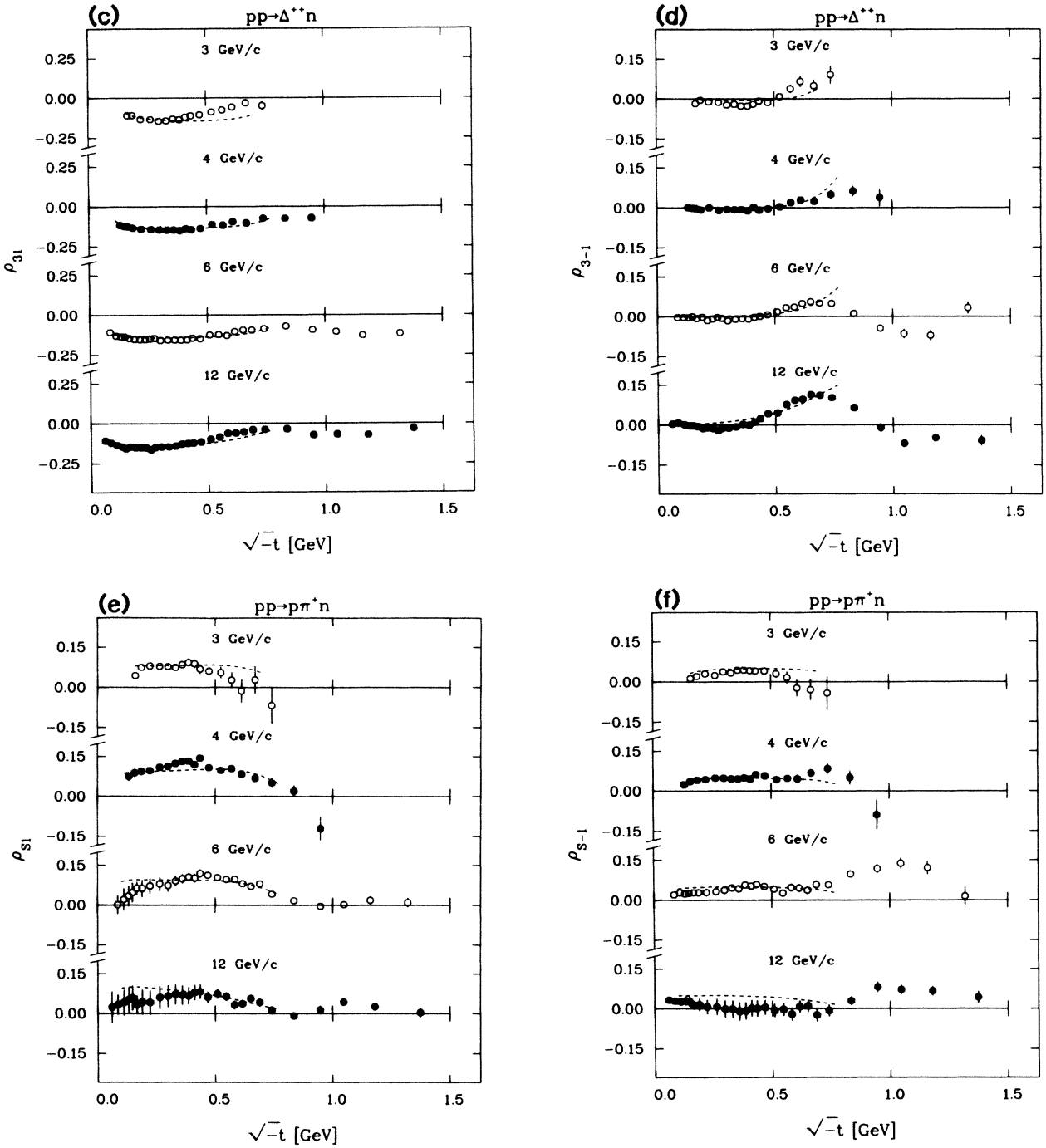

FIG. 7. (*Continued*).

dependence for ρ_{11} for $-t<0.2$ GeV^2, together with the WM prediction.

For small t, the helicity-conserving amplitudes s^1, p^1, and Δ^1 are expected to dominate in the WM, and consequently the main polarization contributions from s-Δ interference are expected to arise in $P_y\rho_{s-1}$ and $P_x\rho_{s-1}$ [cf. Eqs. (20p) and (20q)]. These are plotted against $\sqrt{-t}$ in Fig. 10 in the s channel (open circles for $P_y\rho_{s-1}$, solid circles for $P_x\rho_{s-1}$), together with the WM predictions. They are approximately mirror symmetric, as expected, and independent of $p_{\rm lab}$. The same quantities are shown as functions of mass in Fig. 11, for $-t<0.2$ GeV^2. Note that they vary rather slowly with mass in the Δ^{++} band; it is a trivial exercise to show that $\mathrm{Im}(s^*\Delta)/|\Delta|^2$ would be constant if the s wave were constant with mass and mainly real, as is approximately the case. We remark that the t-channel behavior of these quantities is quite similar. The other s-Δ spin asymmetries are shown as functions of $\sqrt{-t}$ in Figs. 12(a) ($P_y\rho_{s1}$) and 12(b) ($P_z\rho_{s-1}$), in the s channel. These are expected to be small in the WM, but given the rather complicated makeup of these DME's [Eqs. (20o) and (20r)], it is perhaps not surprising that the

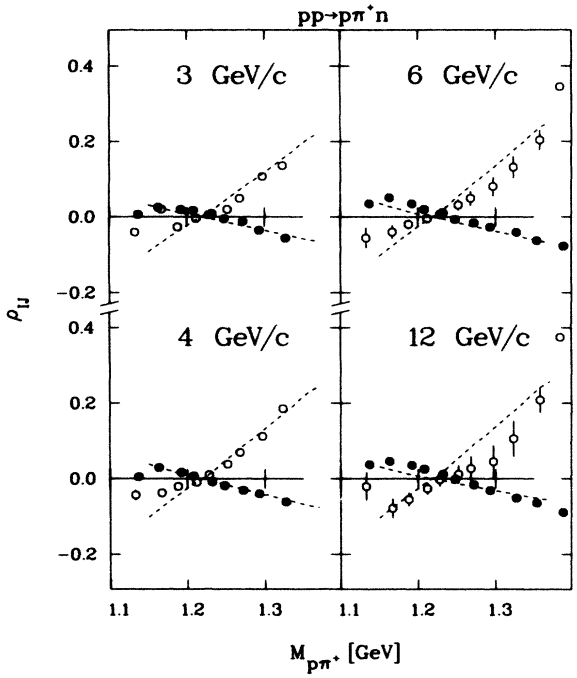

FIG. 8. s-channel ρ_{s1} (open circles) and ρ_{s-1} (solid circles), with WM predictions (dashed curves), as functions of mass.

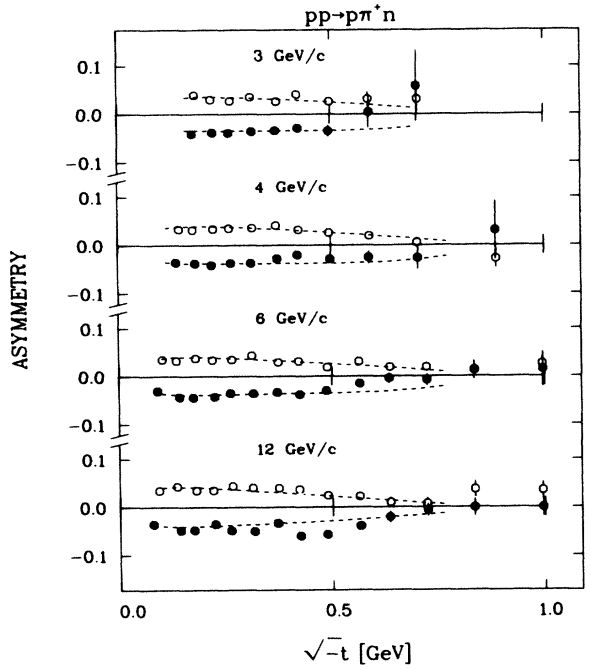

FIG. 10. s-channel $P_y\rho_{s-1}$ (open circles) and $P_x\rho_{s-1}$ (solid circles), with WM predictions (dashed curves), plotted against $\sqrt{-t}$.

WM predictions are only qualitatively successful.

Figures 13(a)—13(h) show the s-channel spin correlations against t for the DME's which involve Δ-Δ or p-Δ interferences: $P_y\rho_{11}$ (a), $P_y\rho_{33}$ (b), $P_y\rho_{31}$ (c), $P_y\rho_{3-1}$ (d), $P_x\rho_{31}$ (e), $P_x\rho_{3\text{-}1}$ (f), $P_z\rho_{31}$ (g), and $P_z\rho_{3-1}$ (h). The solid curves are polynomial interpolations chosen to be identical at all four energies, for each DME, just as in Fig. 5; it is obvious that none of the DME's shows any striking departure from the "standard" shape as a function of p_{lab}. The dashed curves in Figs. 13(a)—13(h) show the WM predictions for the 6-GeV/c data, based solely on the expected p-Δ interference. As noted above [Eq. (22a)], $P_y\rho_{31}$ and $P_x\rho_{31}$ need not vanish at $t'=0$, because they include mirror-symmetric contributions from $\text{Im}(p^{1*}\Delta^1)$

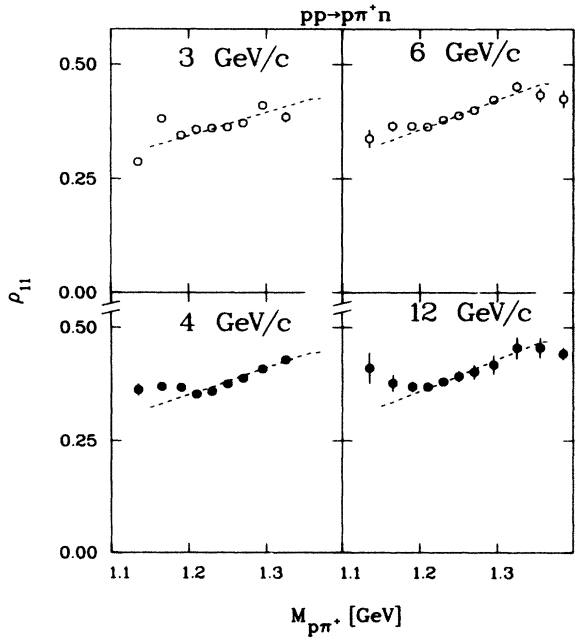

FIG. 9. s-channel ρ_{11}, with WM predictions (dashed curves), as functions of mass.

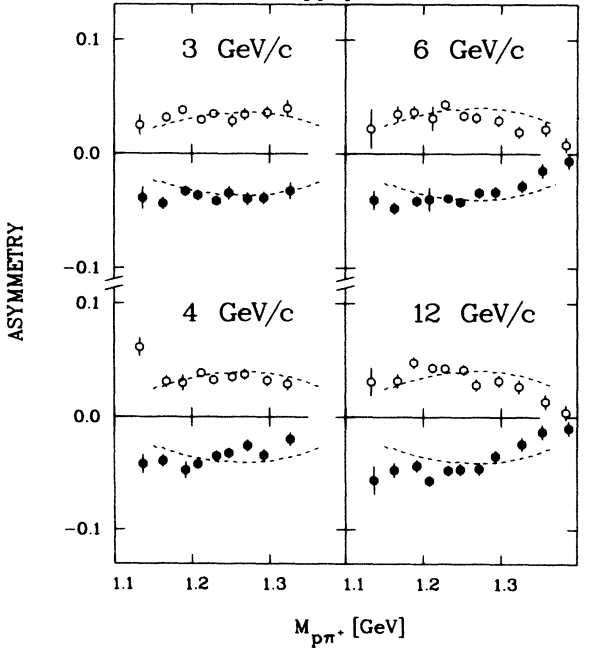

FIG. 11. s-channel $P_y\rho_{s-1}$ (open circles) and $P_x\rho_{s-1}$ (solid circles), with WM predictions (dashed curves), as functions of mass.

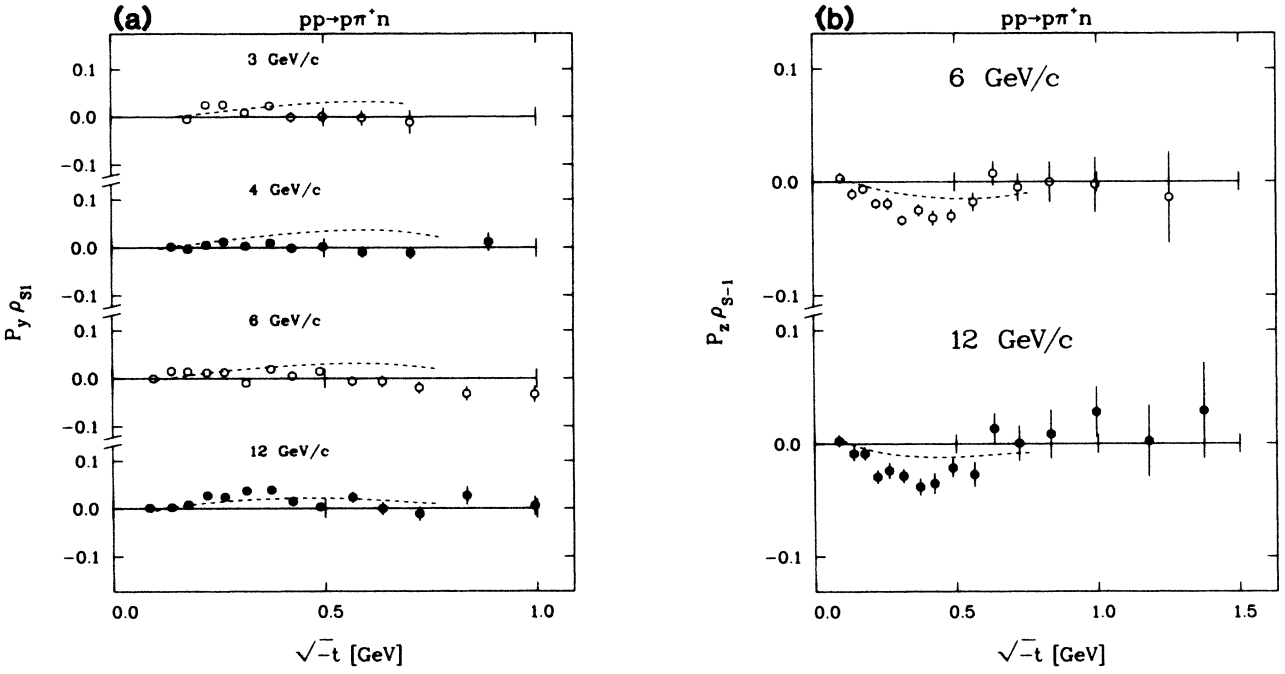

FIG. 12. (a) s-channel $P_y\rho_{s1}$, with WM predictions (dashed curves), plotted against $\sqrt{-t}$. (b) s-channel $P_z\rho_{s-1}$, as in (a).

[Eqs. (20g) and (20i)]; this is reflected in the dashed curves and seems to be approximately valid at small t [Figs. 13(c) and 13(e)]. This behavior is analogous to that of $P_y\rho_{s-1}$ and $P_x\rho_{s-1}$ in Fig. 10, which receive equal and opposite contributions from $\mathrm{Im}(s^{1*}\Delta^1)$.

The t-channel spin correlations do not offer any striking simplifications. Figures 14(a) and 14(b) show $P_y\rho_{11}$ and $P_y\rho_{33}$ in the t channel, with analogous solid and dashed curves as in Fig. 13. The important point to note is that the $p^*\Delta$ terms (e.g., the dashed curves) do not ac-

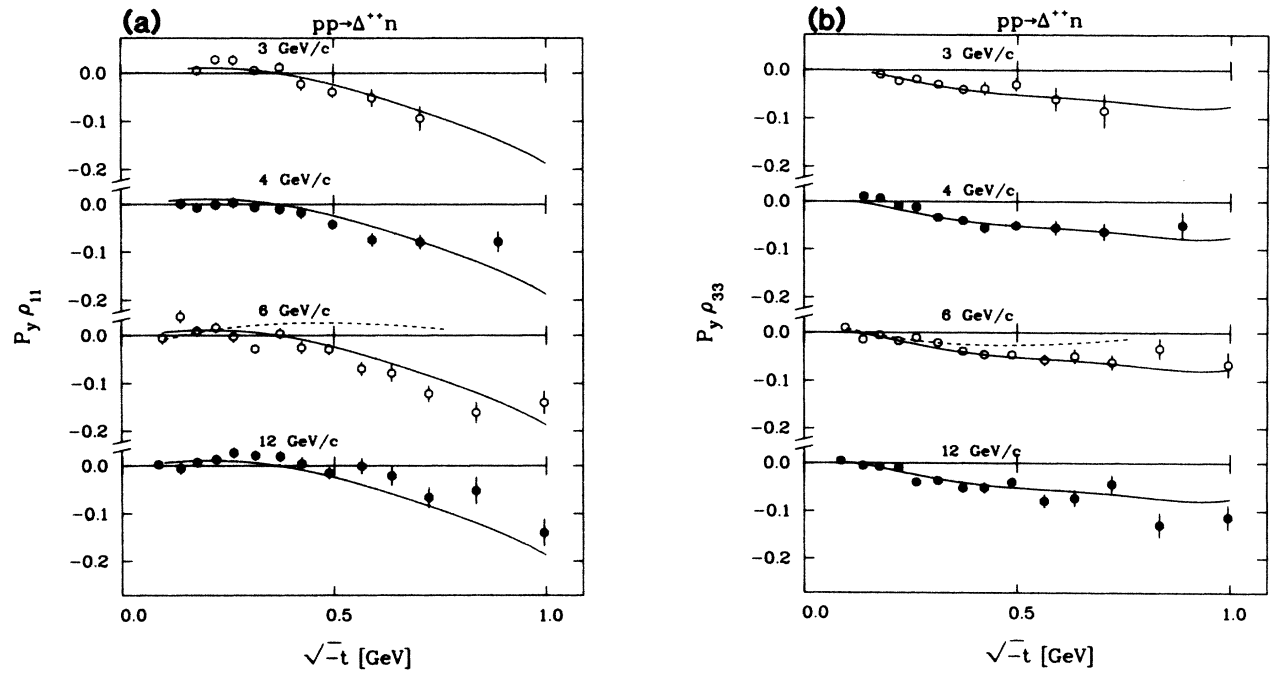

FIG. 13. (a) s-channel $P_y\rho_{11}$ plotted against $\sqrt{t}$. The solid curves are a fixed polynomial, based on an average of the 6- and 11.75-GeV/c data. The dashed curve at 6 GeV/c gives the WM prediction, based on the p-Δ interference contribution. (b) s-channel $P_y\rho_{33}$, as in (a). (c) s-channel $P_y\rho_{31}$, as in (a). (d) s-channel $P_y\rho_{3-1}$, as in (a). (e) s-channel $P_x\rho_{31}$, as in (a). (f) s-channel $P_x\rho_{3-1}$, as in (a). (g) s-channel $P_z\rho_{31}$, as in (a). (h) s-channel $P_z\rho_{3-1}$, as in (a).

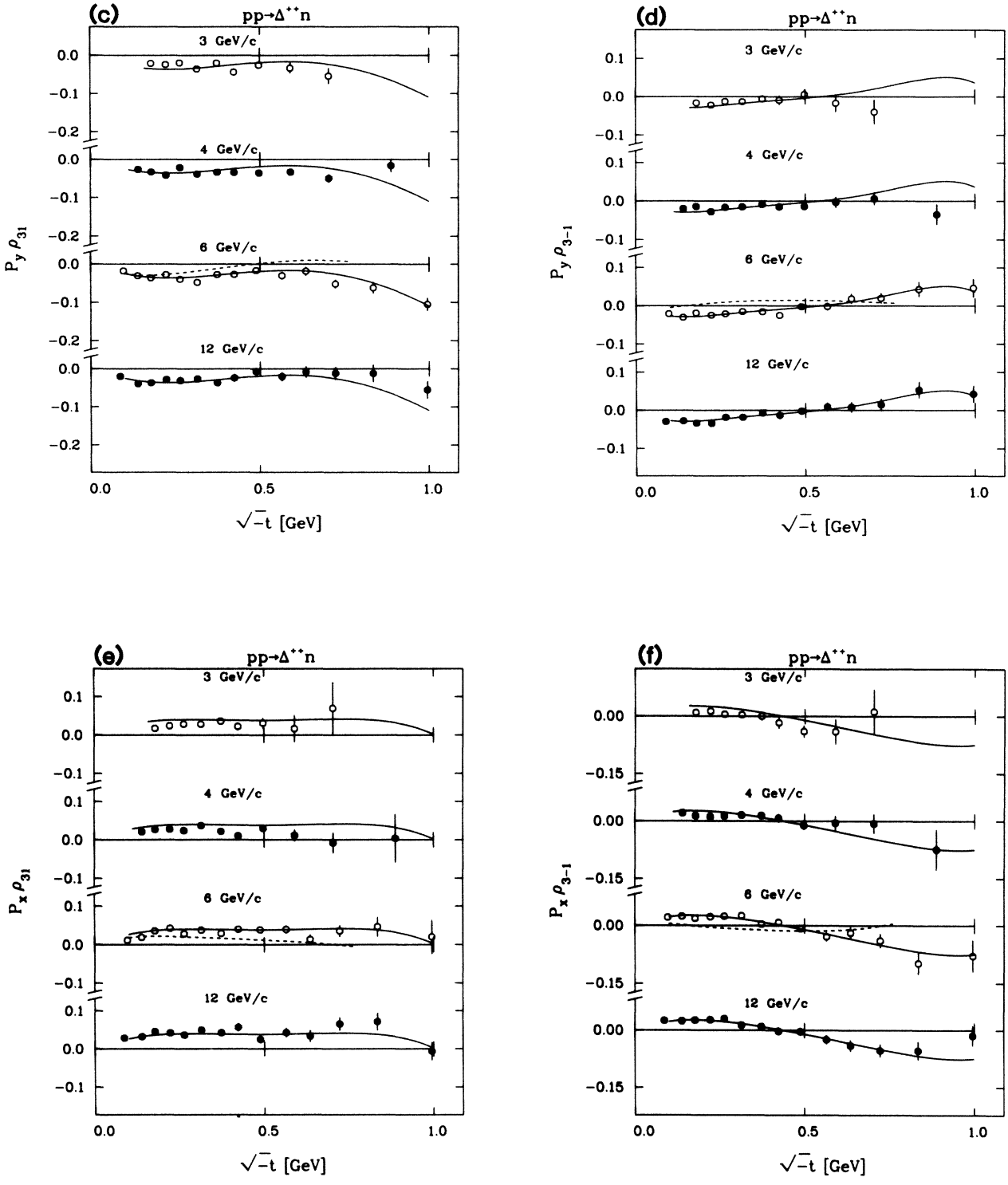

FIG. 13. (*Continued*).

count fully for any of these DME's, and it is clear that $\Delta^*\Delta$ contributions are needed. This is not surprising in view of the large left-right asymmetry (Fig. 5), which must be almost entirely due to $\Delta^*\Delta$ interference (e.g., ignoring p^*p and s^*s contributions).

As noted above [cf. Eq. (23)], we can test for the naturality contributions by comparing the P_x and P_z observables. This comparison is shown in Figs. 15(a) (6 GeV/c, s channel), 15(b) (12 GeV/c, s channel), 16(a) (6 GeV/c, t channel), and 16(b) (12 GeV/c, t channel). The approximate mirror symmetry of $P_x\rho_{31}$ and $P_z\rho_{3-1}$, and of $P_x\rho_{3-1}$ and $-P_z\rho_{31}$, suggests dominance of *UP* ex-

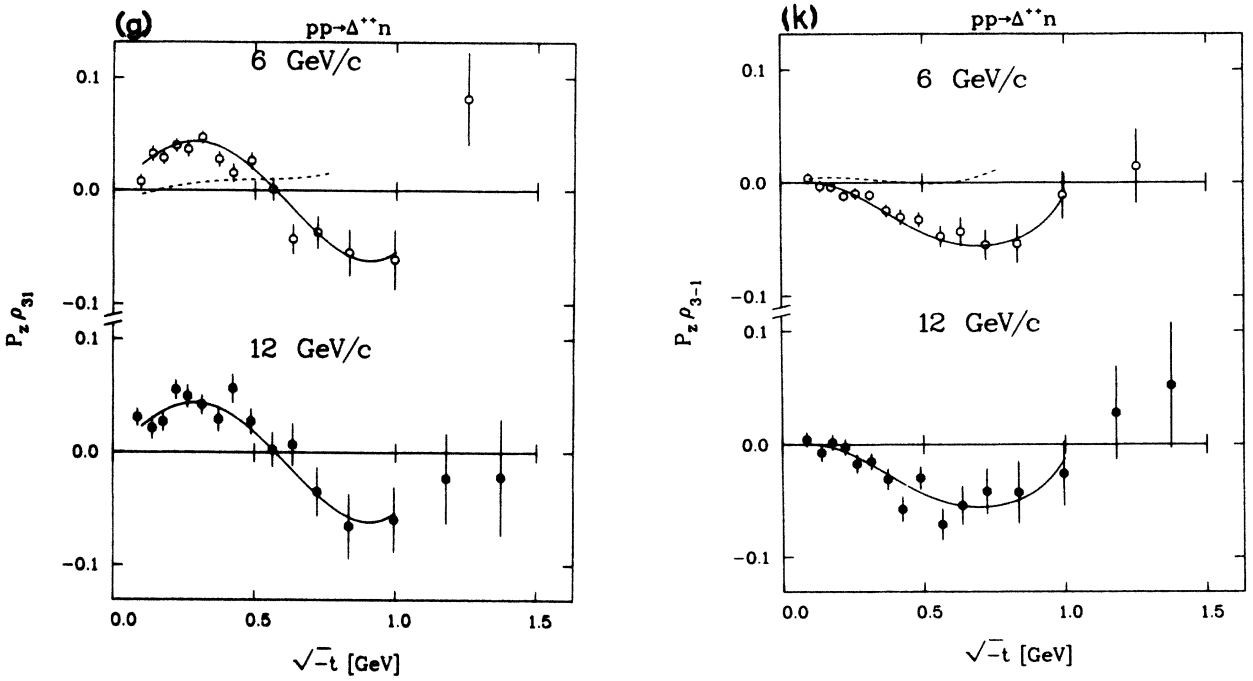

FIG. 13. (*Continued*).

changes. We have subtracted the small $p^*\Delta$ interference contributions from these DME's, using the WM; the solid curves are polynomial fits to guide the eye (they are virtually identical at the two energies). This mirror symmetry, together with the large value of the integrated asymmetry, $2(P_y\rho_{11}+P_y\rho_{33})$, is in our view the most incisive result of the experiment. It suggests that the *NP* contributions to the spin correlations are small at these energies, and that the spin dependence in the $\Delta^*\Delta$ terms arises mainly from interference of π and B exchange. It turns out that there is a natural explanation for this in the simple additive quark model.

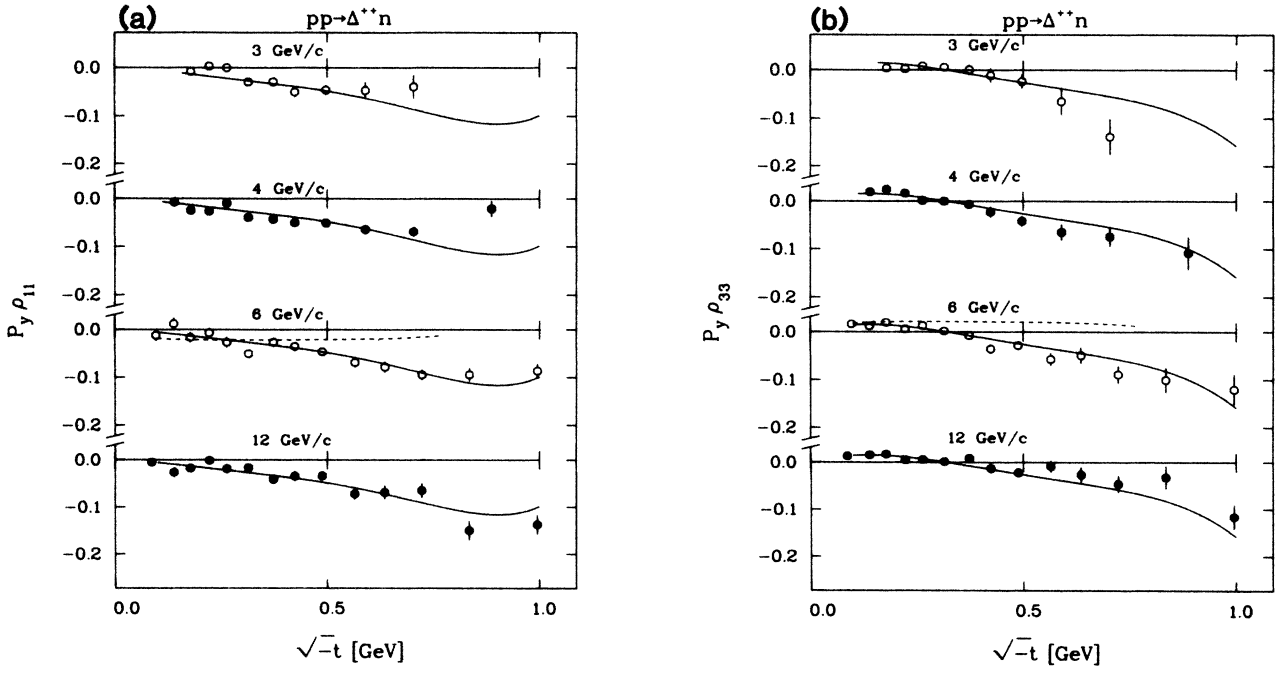

FIG. 14. (a) t-channel $P_y\rho_{11}$, as in 13(a). (b) t-channel $P_y\rho_{33}$, as in 13(d).

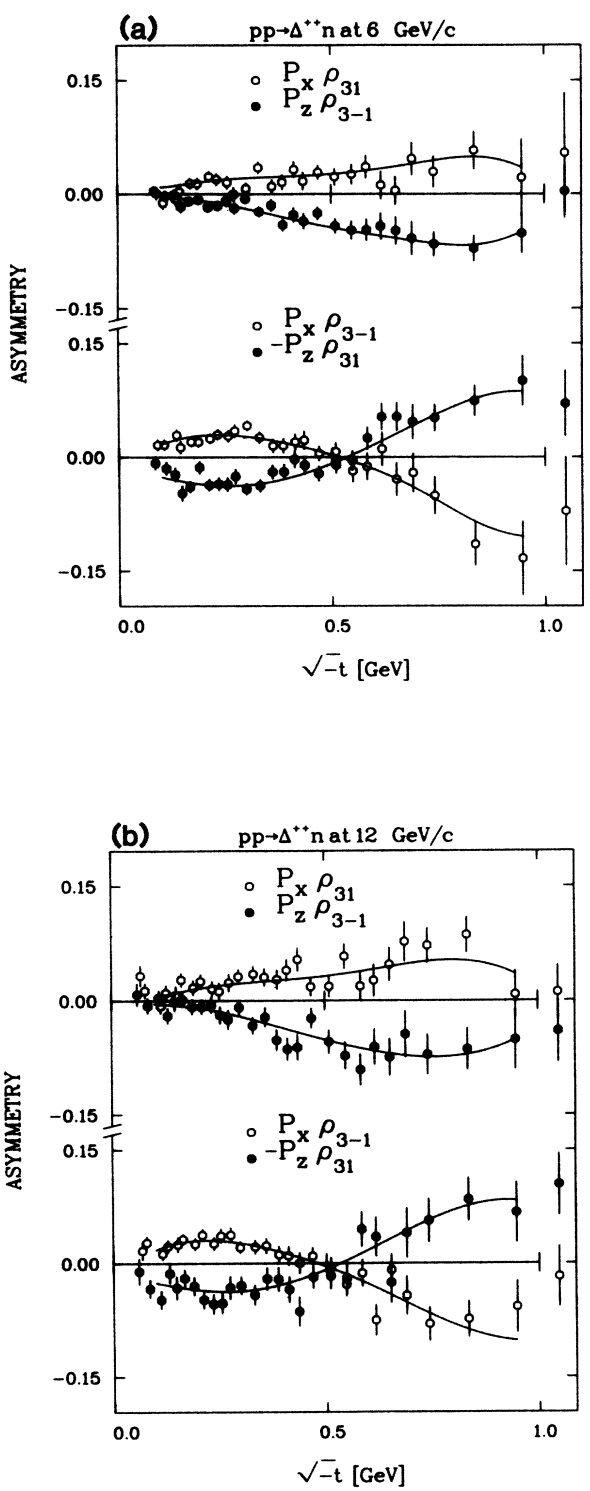

FIG. 15. (a) s-channel P_x (open circles) and P_z (solid circles) correlations at 6 GeV/c. The points have been corrected for the p-Δ interference contributions, predicted by the WM. The solid curves are polynomial fits based on an average of the 6- and 11.75-GeV/c DME's, again with the p-Δ interference terms subtracted. We have included an overall minus sign for $P_z\rho_{31}$, so that the P_x and P_z correlations would be mirror symmetric for pure UP exchange, and identical for pure NP. (b) s-channel P_x and P_z correlations at 11.75 GeV/c, as in (a).

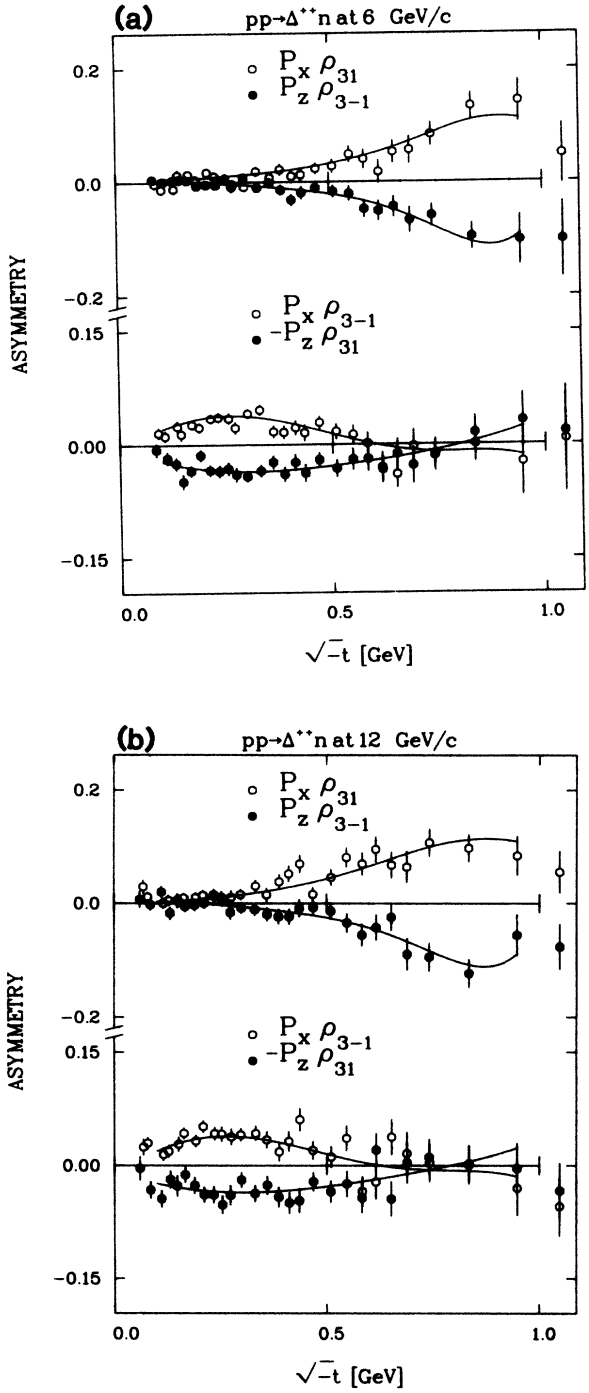

FIG. 16. (a) t-channel P_x and P_z correlations at 6 GeV/c, as in 15(a). (b) t-channel P_x and P_z correlations at 11.75 GeV/c, as in 15(a).

V. PHENOMENOLOGICAL CONSIDERATIONS

A. Quark-model relations

There are constraints from the additive quark model[18] (AQM) that relate the Δ-production amplitudes to each other and to amplitudes for CEX vector-meson production; the latter arise from the close analogy between the CEX transitions $p \to \Delta^{++}$ and, e.g., $K^+ \to K^{*0}$, which in-

volve $^1S_0 \to {}^3S_1$ transitions for qq and $q\bar{q}$ pairs, respectively. The relations involving Δ-production amplitudes alone are

$$N^3 = \sqrt{3} N^{-1} , \tag{25a}$$

$$U^3 = -\sqrt{3} U^{-1} , \tag{25b}$$

$$N^{-3} = U^{-3} = N^1 = 0 . \tag{25c}$$

[Henceforth, we use N^M and U^M as in Eq. (17) to denote Δ-production amplitudes; they are normalized to give the total Δ-production cross sections, integrated over $M_{p\pi^+}$, and so we suppress the explicit $M_{p\pi^+}$ dependence of Eq. (A1).] These relations are approximately satisfied by our WM parametrization. Equation (25c) is built into the t-channel amplitude description, and the factor $\sqrt{3}$ in Eqs. (25a) and (25b) is approximately valid for small t [the exact factor, based on Eq. (A9) and Table I, ranges from 1.3 to 1.4 near $t'=0$]. The relations (25a) and (25b) are also approximately valid in the s channel in the WM; however, small U^{-3}, N^{-3}, and N^1 amplitudes arise in the s channel, subject to the constraint

$$N^{-3} \approx \sqrt{3} N^1 \simeq -0.4 (t - t_{\min})^{1/2} N^3 . \tag{25d}$$

The predicted relations between $pp \to \Delta^{++} n$ and $K^+ n \to K^{*0}(890) p$ can be written

$$P_+(K^*) = N^3(\Delta) , \tag{26a}$$

$$P_-(K^*) = U^3(\Delta) , \tag{26b}$$

$$P_0(K^*) = (\tfrac{3}{4})^{1/2} U^1(\Delta) , \tag{26c}$$

where the K^{*0}-production amplitudes are normalized as in Ref. 7, namely,

$$\sigma(K^*) = |P_+|^2 + |P_-|^2 + |P_0|^2 . \tag{27}$$

Thus, with the Δ-production amplitudes normalized as in Eq. (19), the cross-section relations are

$$\sigma(K^*) = \tfrac{3}{8} \sigma(\Delta) . \tag{28}$$

We use Eqs. (25a)–(25c) to decompose the Δ-production cross sections into

$$\sigma_+(\Delta) = \tfrac{4}{3} \sigma(\rho_{33} + \sqrt{3} \rho_{3-1}) = 2(|N^3|^2 + |N^{-1}|^2) , \tag{29a}$$

$$\sigma_-(\Delta) = \tfrac{4}{3} \sigma(\rho_{33} - \sqrt{3} \rho_{3-1}) = 2(|U^3|^2 + |U^{-1}|^2) , \tag{29b}$$

$$\sigma_0(\Delta) = 2\sigma \left[\rho_{11} - \frac{\rho_{33}}{3} \right] = 2 |U^1|^2 , \tag{29c}$$

so that

$$\sigma(\Delta) = \sigma_+(\Delta) + \sigma_-(\Delta) + \sigma_0(\Delta) \tag{30}$$

and, in the AQM,

$$\sigma_{+,-,0}(\Delta) = \tfrac{8}{3} \sigma_{+,-,0}(K^{*0}) . \tag{31}$$

The three projections for the Δ^{++} cross sections are shown for 6 and 12 GeV/c in Figs. 17(a) and 17(b) (s channel) and Figs. 18(a) and 18(b) (t channel), with polynomial curves to guide the eye. The *NP* projection σ_+ is frame invariant; Fig. 19 shows σ_+ as a fraction of the total Δ-production cross section at 4, 6, and 12 GeV/c. Note the following features: (a) σ_- exhibits a sharp dip in the s channel near $-t = m_\pi^2$, as expected from the WM; (b) σ_+ shows a break in the t dependence around $-t = 0.1$ GeV^2, having a steep t dependence consistent with pion exchange for small t ($e^{\sim 17t}$), and a very shallow dependence characteristic of ρ and A_2 exchange for larger t ($e^{\sim 3t}$); (c) σ_- and σ_0 have very similar t dependence in the t channel, as expected in the WM; (d) σ_+ has a strong

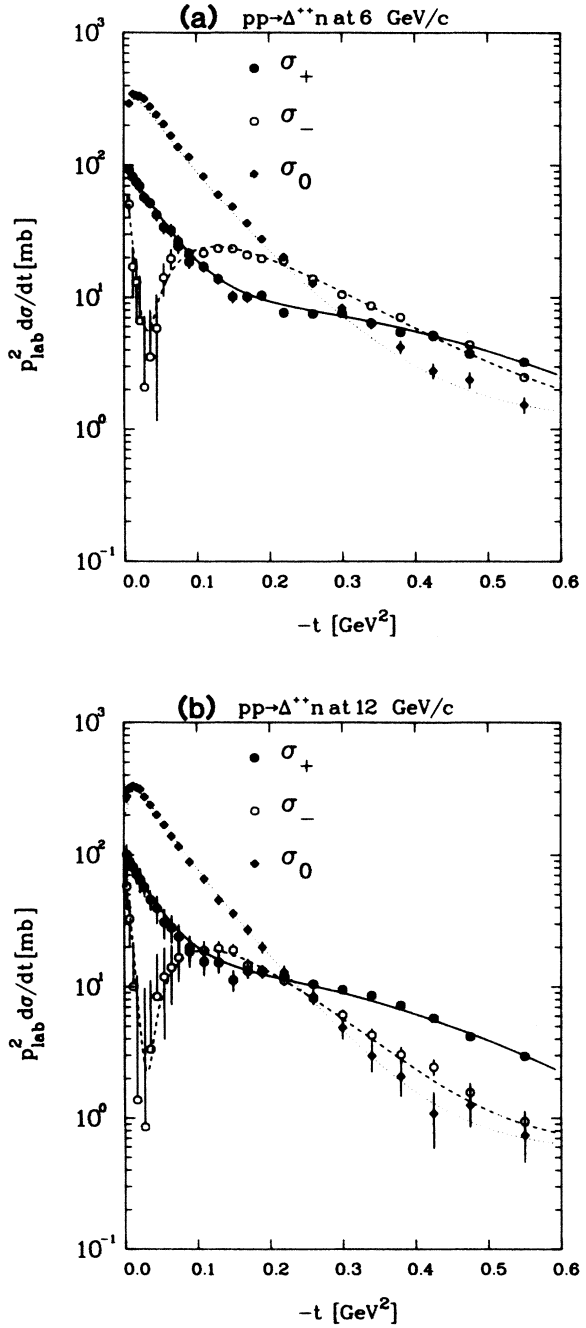

FIG. 17. (a) *NP* (σ_+) and *UP* (σ_-,σ_0) projections at 6 GeV/c, plotted against t, in the s channel. The projections are obtained from the AQM, and are defined in the text. The sum of the projections gives the forward differential cross section $p_{\rm lab}{}^2 d\sigma/dt$ corrected for the Δ^{++} tail outside the selection band (1.15–1.34 GeV). (b) *NP* and *UP* projections at 11.75 GeV/c, as in (a), in the s channel.

energy dependence relative to σ_- and σ_0.

Figure 20 shows a comparison of the s-channel projections for $pp \to \Delta^{++} n$, $\pi^- p \to \rho^0(770) n$, and $K^+ n \to K^{*0}(890) p$; we display polynomial interpolations of these quantities at 6 GeV/c, using data from Ref. 7. We have normalized the ρ^0 and K^{*0} cross sections to obtain agreement with $\sigma_0(\Delta)$ at small t; the normalization factor needed for K^{*0} is about twice that predicted by relation (31). We note that all three reactions have similar t dependence and exhibit similar break structures in σ_+. Similar comparisons for unpolarized Δ and K^{*0} produc-

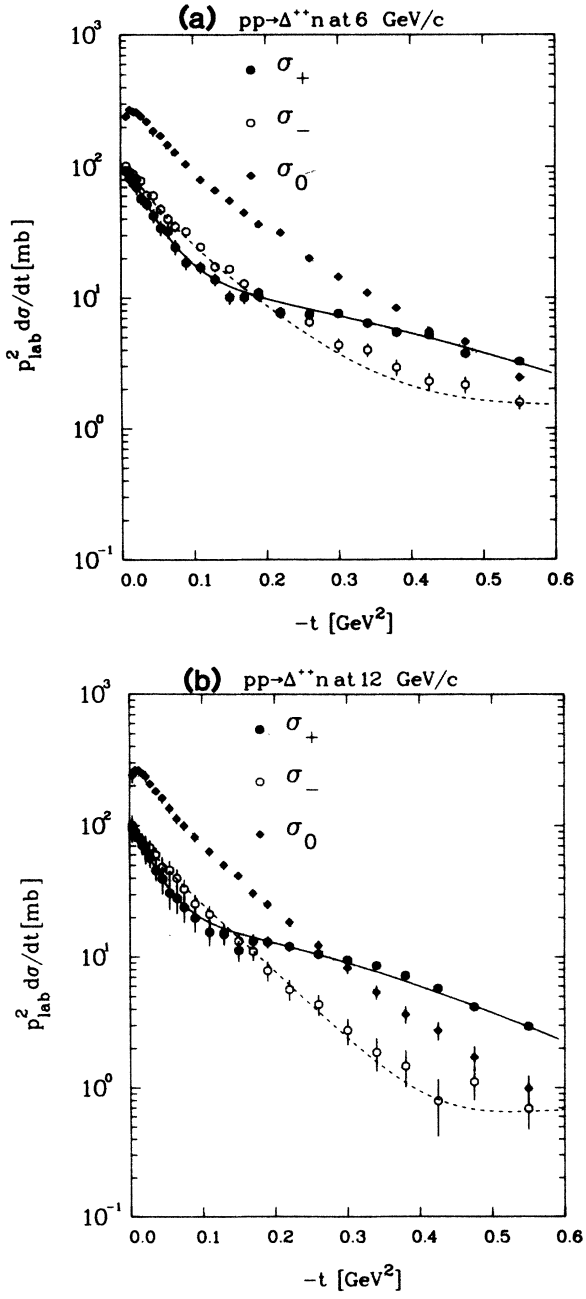

FIG. 18. (a) *NP* and *UP* projections at 6 GeV/c, as in 17(a), in the t channel. (b) *NP* and *UP* projections at 11.75 GeV/c, as in 17(a), in the t channel.

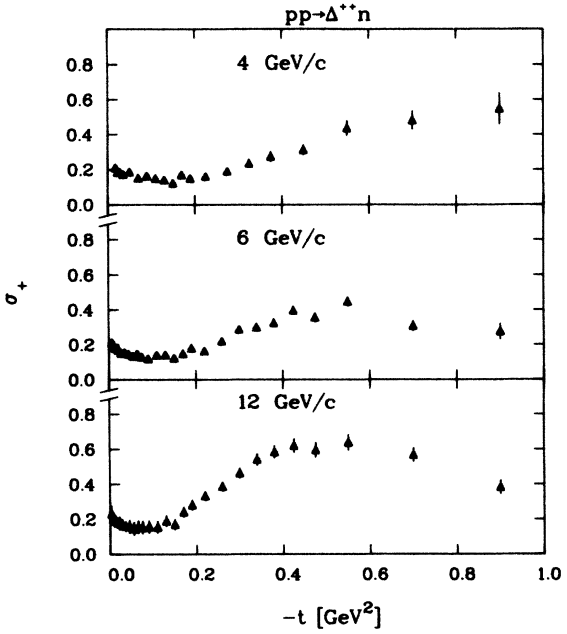

FIG. 19. The fraction $\sigma_+/(\sigma_+ + \sigma_- + \sigma_0)$, plotted against t at 4, 6, and 11.75 GeV/c, as obtained from the AQM relations.

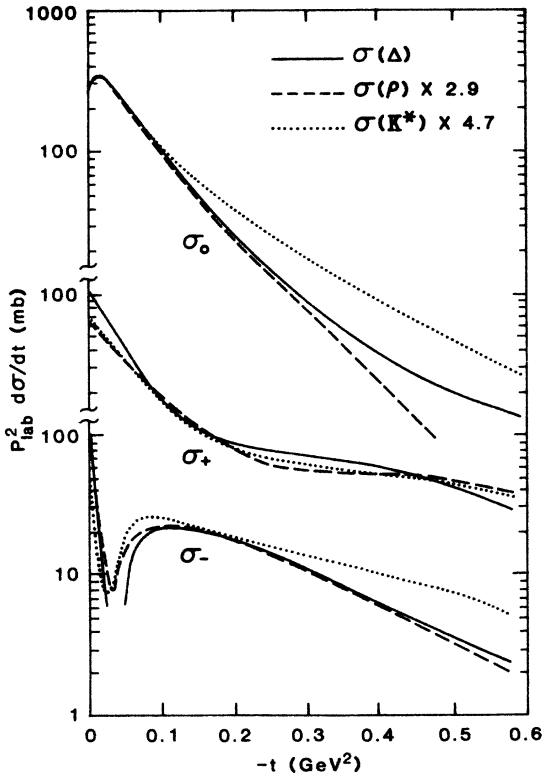

FIG. 20. The *NP* (σ_+) and *UP* (σ_- and σ_0) Δ^{++}-production cross sections in the s channel (solid curves), plotted against t for 6 GeV/c. For comparison, the dashed (dotted) curves show the σ_+, σ_-, and σ_0 cross sections for $\pi^- p \to \rho^0 n$ ($K^+ n \to K^{*0} p$), normalized to obtain agreement in σ_0 at small t. The curves are polynomial interpolations of data from this experiment and Ref. 7.

tion have been given by Field[18] and Itano *et al.*[18] Also, amplitude analysis of K^{*0} production with a polarized target has been reported by de Lesquen *et al.*,[19] and these data, together with the present experiment, in principle, permit more detailed tests of the AQM relations.

B. Energy dependence

We show $\alpha_{\text{eff}}(t)$ for the Δ-production cross sections in Fig. 21, based on fits to the 6- and 12-GeV/c data (inclusion of the 3- and 4-GeV/c data does not change these results significantly). We find that σ_0 and σ_- have $\alpha_{\text{eff}} \approx t$ (solid curves), while σ_+ switches from $\alpha_{\text{eff}} \approx t$ for $-t < 0.1$ GeV^2 to $\alpha_{\text{eff}} \approx 0.45 + t$ for $-t > 0.2$ GeV^2. The latter behavior is obviously correlated with the break in the σ_+ t dependence shown in Figs. 17 and 18. Figure 22 shows the forward differential cross section for Δ^{++} production in reaction (2) at 1500 GeV/c from de Kerret *et al.*[2,20] The upper curve in Fig. 22 shows a smooth interpolation of the 1500-GeV/c cross section; the lower curve is just an extrapolation of the upper curve from 1500 to 6 GeV/c, using $p_{\text{lab}}^{2\alpha_{\text{eff}}(t)}$, with $\alpha_{\text{eff}} = 0.45 + t$ (GeV^2). This extrapolation describes the 6-GeV/c σ_+ data fairly well for $-t > 0.15$ GeV^2. It seems clear that the sharp forward peak in σ_+ at 6 GeV/c is due mainly

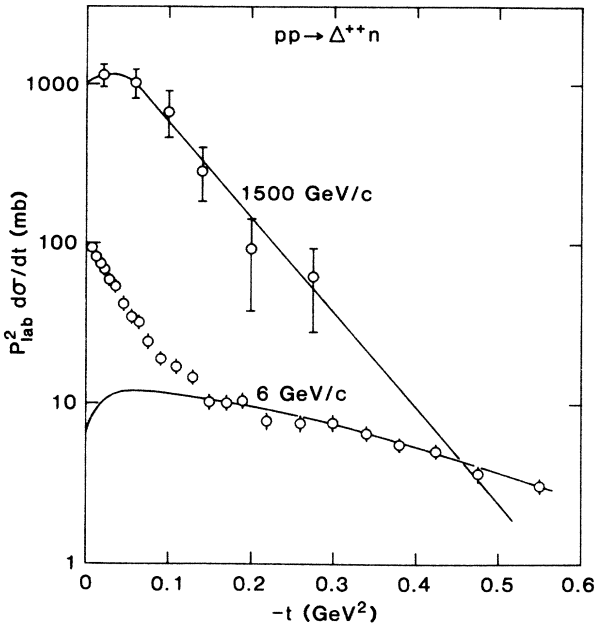

FIG. 22. The total $p_{\text{lab}}{}^2 d\sigma/dt$ at 1500 GeV/c (open circles) obtained by de Kerret *et al.* (Refs. 2 and 18) with smooth interpolation (top curve), and σ_+ at 6 GeV/c obtained from the AQM (solid circles); the 6-GeV/c curve is just the 1500-GeV/c curve scaled by $(p_{\text{lab}})^{2\alpha_{\text{eff}}(t)}$, where $\alpha_{\text{eff}}(t) = 0.45 + t$.

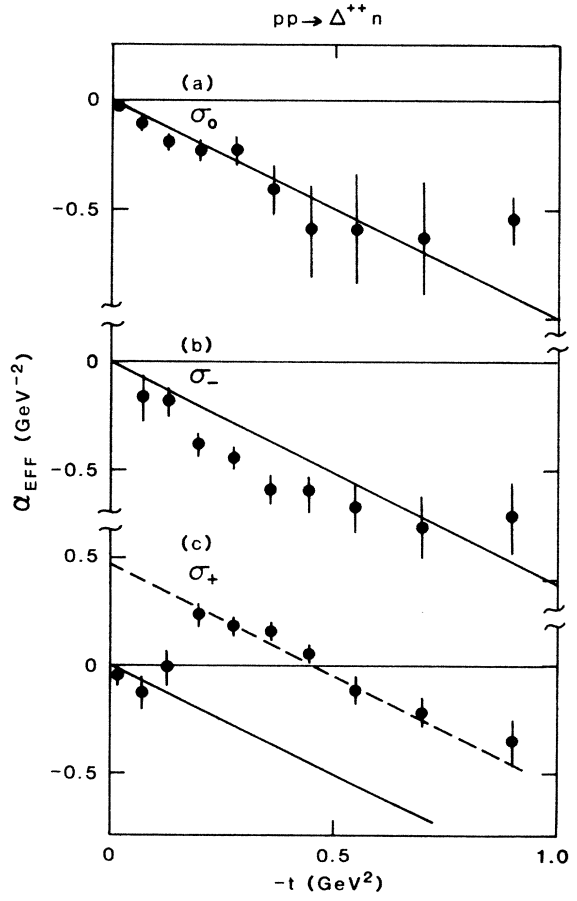

FIG. 21. Effective trajectories for the σ_0, σ_-, and σ_+ projections, based on fits of the form $p_{\text{lab}}{}^2 d\sigma/dt \propto (p_{\text{lab}})^{2\alpha_{\text{eff}}(t)}$. The solid lines give $\alpha(t) = t$; the dashed line gives $\alpha(t) = 0.45 + t$.

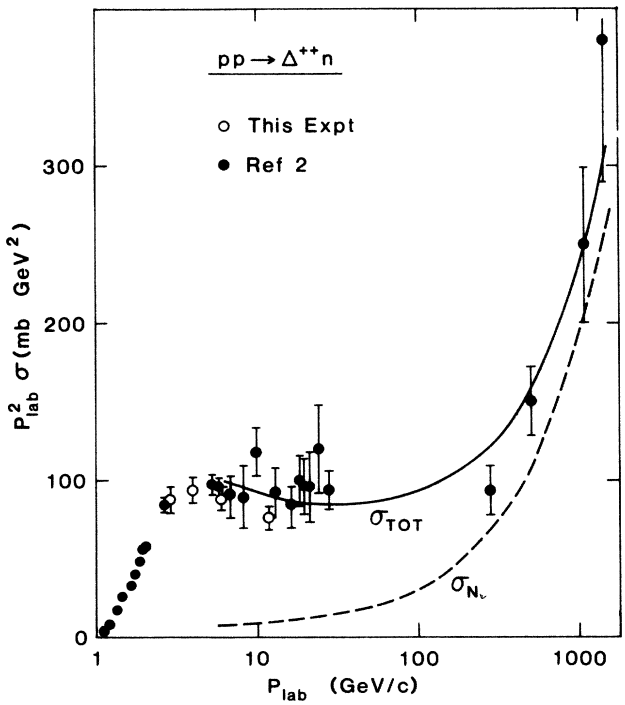

FIG. 23. Total cross sections for $pp \to \Delta^{++} n$ from this experiment (open circles) and from experiments listed in Ref. 2 (solid circles). The points above 100 GeV/c are those reported by de Kerret *et al.* The dashed curve is our estimate for the *NP* cross section extrapolating the high-energy data with $\alpha_{\text{eff}}(t) = 0.45 + t$. The solid curve is the total Δ-production cross section obtained by extrapolating 6-GeV/c σ_0 and σ_-, using $\alpha_{\text{eff}}(t) = t$, added to the *NP* estimate.

to the pion-exchange cut; because of its lower α_{eff}, it is essentially absent in the 1500-GeV/c data. Figure 23 shows total Δ^{++} production cross sections for reaction (2) from threshold to ISR energies, using the data of Ref. 2 as well as this experiment. (These cross sections are doubled, as compared with the forward cross sections shown elsewhere in this paper, to account for target fragmentation.) The dashed and solid curves indicate our estimate for the *NP* contribution and the total. We took the *NP* cross section from the 1500-GeV/c data, extrapolated downward in p_{lab} using $\alpha_{\text{eff}}=0.45+t$, as in Fig. 22. We extrapolated σ_0, σ_-, and forward σ_+ upwards from 6 GeV/c, using $\alpha_{\text{eff}}(t)=t$ as obtained from the 6- and 12-GeV/c comparison, and thus obtained the total Δ-production cross-section curve. A similar decomposition has been given by Moriarty and Navelet.[20]

C. Amplitude structure

In trying to arrive at a plausible understanding of the amplitude structure, we are guided by the following clues: (a) the dominance of *UP* contributions in the P_x and P_z spin correlations; (b) the WM features observed at small t, in particular, the evidence for crossover zeros in U^3 and U^{-1}; (c) the empirical energy dependence of σ_+ and the related break structure in t; and (d) the AQM relations and the qualitative similarities between vector-meson and Δ^{++} production. Combining these ideas, we can summarize the AQM relations [Eq. (26)] as

$$N^3=\sqrt{3}N^{-1}\approx\frac{[P_+(\rho_0)+P_+(\omega)]}{\sqrt{2}}=A_2+\rho+\pi_{\text{cut}}\ , \tag{32a}$$

$$U^3\simeq-\sqrt{3}U^{-1}\approx\frac{[P_-(\rho^0)+P_-(\omega)]}{\sqrt{2}}=\pi_-+B_-\ , \tag{32b}$$

$$U^1\approx(\tfrac{2}{3})^{1/2}[P_0(\rho^0)+P_0(\omega)]=\pi_0+B_0\ , \tag{32c}$$

where we have used SU(3) relations to express the K^{*0} amplitudes of Eq. (26) in terms of those for ρ^0 and ω production, e.g.,

$$(K^*n\to K^{*0}p)=\frac{(\pi^-p\to\rho^0n)+(\pi^-p\to\omega n)}{\sqrt{2}}\ . \tag{33}$$

The relevant exchanges are given on the RHS of Eq. (32), e.g., π, π_{cut}, and A_2 for ρ^0 production and B and ρ for ω production. The relative phases of the ρ^0- and ω-production amplitudes are known from ρ-ω interference measurements,[7] and they are generally consistent with the phases expected for the exchange contributions. Even though the individual exchange contributions to the *NP* amplitudes have presumably very different phases, the relation $N^3=\sqrt{3}N^{-1}$ results in phase coherence for the *NP* amplitudes and explains the absence of *NP* spin-correlation effects. Spin dependence can arise in the *UP* sector because U^1 and $U^3\approx-\sqrt{3}U^{-1}$ are independent and can have different phases, provided, e.g.,

$$\frac{B_0}{\pi_0}\neq\frac{B_-}{\pi_-}\ . \tag{34}$$

For ω and ρ^0 production, it is found empirically that the LHS of (34) is much larger than the RHS, in the s channel[7] (the opposite is true in the t channel). Furthermore, the ρ-ω interference phases show that π_0 is $\sim 90°$ ahead of B_0 in the s channel. Thus, at larger t where B exchange becomes important, we would expect relative phases of 0°, $\sim -45°$, and 180° for s-channel U^3, U^1, and U^{-1}, respectively [setting $B_-=0$ and $|B_0|\approx|\pi_0|$ in Eq. (32)]. This is qualitatively what we find.

To proceed further, we assume spin coherence at the recoil-nucleon vertex for larger t; specifically, we assume that the N_{++} and U_{++} amplitudes vanish in the s channel, except for those required in the WM [Eq. (A5a)]. We also assume that s- and p-wave production is given by the WM, leaving eight amplitudes, N^M_{-+} and U^M_{-+}, to be determined for Δ production. We can define the *NP* and *UP* projections of the P_x and P_z observables as

$$N_{31}=P_x\rho_{31}+P_z\rho_{3-1}\ , \tag{35a}$$

$$N_{3-1}=P_x\rho_{3-1}-P_z\rho_{31}\ , \tag{35b}$$

$$U_{31}=P_x\rho_{31}-P_z\rho_{3-1}\ , \tag{35c}$$

$$U_{3-1}=P_x\rho_{3-1}+P_z\rho_{31}\ . \tag{35d}$$

Figure 24 shows the s-channel spin-correlation DME's for the Δ-Δ interference terms at 6 GeV/c; for illustration we have subtracted the p-Δ contributions using the WM and show the polynomial interpolations of the data. The results are similar at 12 GeV/c, except that $P_y\rho_{11}$ is systematically smaller and $P_y\rho_{33}$ larger. Note that the *NP* projections N_{31} and N_{3-1} are small [Fig. 24(d)]; also $U_{31}\approx-2P_y\rho_{31}$ [Fig. 24(b)] and $U_{3-1}\approx-2P_y\rho_{3-1}$ [Fig. 24(c)].

We can express the *NP* projections [Eqs. (20i)—(20l)] as

$$\sigma N_{31}=2\,\text{Im}(N^{-1}N^{3*}-N^1N^{-3*})\ , \tag{36a}$$

$$\sigma N_{3-1}=-2\,\text{Im}(N^{-1}N^{-3*}+N^1N^{3*})\ . \tag{36b}$$

The simplest ansatz to obtain $N_{31}\approx N_{3-1}\approx 0$ is to use the

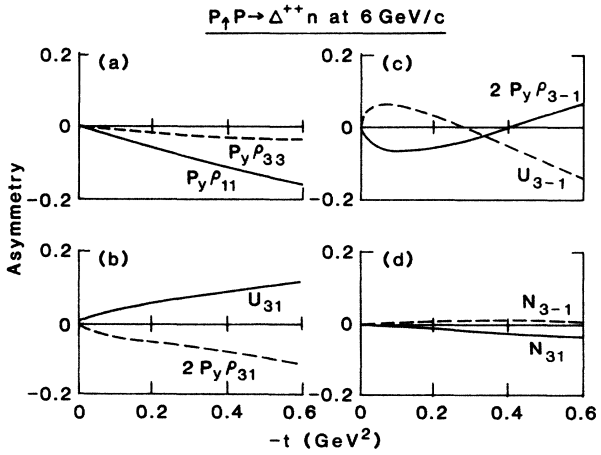

FIG. 24. Polynomial interpolations of the spin correlations at 6 GeV/c which involve $\Delta\Delta$ interference; the $p\Delta$ contributions have been subtracted using the WM parametrization. The observables U_{31}, U_{3-1}, N_{31}, and N_{3-1} are *UP* and *NP* projections based on the P_x and P_z correlations, defined in the text.

AQM constraints. Specifically, we assume two independent NP amplitudes, $N^3=\sqrt{3}N^{-1}$ and $N^{-3}=\sqrt{3}N^1$ [Eq. (25d)]. In that case N_{31} and $N_{3\text{-}1}$ vanish, and there are only two independent NP contributions to the observables, which we can choose to be

$$\sigma_N=|N^3|^2+|N^{-3}|^2\,, \tag{37a}$$

$$\sigma_N A_N=2\,\mathrm{Im}(N^{-3}N^{3*})\,. \tag{37b}$$

We can express the remaining spin observables in terms of the UP amplitudes and A_N as follows:

$$\sigma P_y\rho_{11}=2\,\mathrm{Im}(U^{-1}U^{1*})+\sigma_N A_n/3\,, \tag{38a}$$

$$\sigma P_y\rho_{33}=-2\,\mathrm{Im}U^{-3}U^{3*}+\sigma_N A_N\,, \tag{38b}$$

$$\sigma P_y\rho_{31}=\mathrm{Im}(U^1U^{-3*}+U^{-1}U^{3*})\,, \tag{38c}$$

$$\sigma\tfrac{1}{2}U_{31}=\mathrm{Im}(U^1U^{-3*}-U^{-1}U^{3*})\,, \tag{38d}$$

$$\sigma P_y\rho_{3-1}=\mathrm{Im}(U^{-1}U^{-3*}-U^1U^{3*})+\sigma_N A_N/\sqrt{3}\,, \tag{38e}$$

$$\sigma\tfrac{1}{2}U_{3-1}=\mathrm{Im}(U^{-1}U^{-3*}+U^1U^{3*})\,. \tag{38f}$$

The approximate mirror symmetry of $2P_y\rho_{31}$ and U_{31}, and also $2P_y\rho_{3-1}$ and U_{3-1}, is easily explained if $U^{-3}\approx 0$ in Eqs. (38c) and (38d) and (38e) and (38f). In that case, there would be four independent spin correlations:

$$\sigma P_y\rho_{33}\sim\sigma_N A_N\,, \tag{39a}$$

$$\sigma P_y\rho_{11}\sim 2\,\mathrm{Im}(U^{-1}U^{1*})+\sigma_N A_{N/3}\,, \tag{39b}$$

$$\sigma U_{31}\sim -2\,\mathrm{Im}(U^{-1}U^{3*})\,, \tag{39c}$$

$$\sigma U_{3-1}\sim 2\,\mathrm{Im}(U^1U^{3*})\,, \tag{39d}$$

all of which are nonzero in the data (Fig. 24).

We fitted the s-channel polynomial interpolations at 6 and 12 GeV/c, using the constraints on the NP amplitudes given above.[21] The magnitudes of the independent amplitudes are given in Fig. 25 for 6 GeV/c; N^3 is not determined directly but is defined by $N^3=(\sigma_N)^{1/2}$ from Eq. (37a). For illustrative purposes, we have attached relative phases of 0° or 180° to the amplitudes in Fig. 25 as given by the WM at small t for N^3, U^3, U^{-1}, and U^1; this helps to show the crossover behavior at small t, where the amplitudes are essentially relatively real. The amplitude U^{-3} is fairly small, but is $\sim 180°$ out of phase with respect to U^1 in the fits, as indicated in Fig. 25(a). The 12-GeV/c amplitudes are similar except for the shrinkage

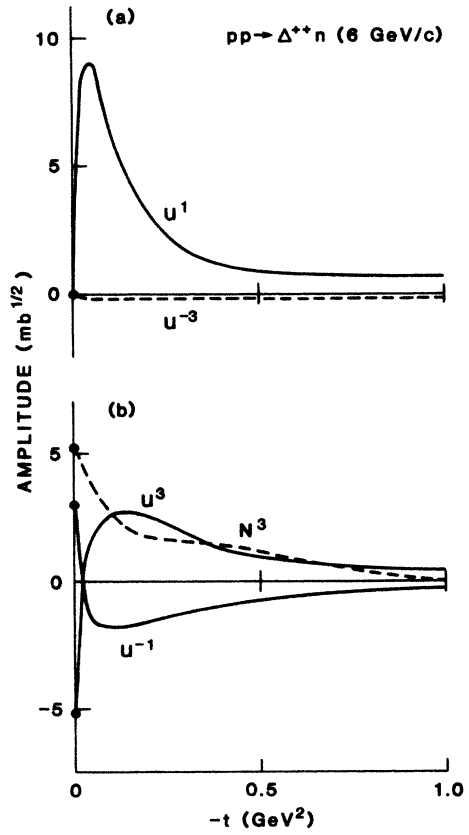

FIG. 25. Magnitudes of the 6-GeV/c Δ^{++}-production amplitudes, U^M_{-+} and N^M_{-+}, from the amplitude analysis described in the text. We have affixed the small-t phases found in the WM fits (e.g., 0° or 180°) to illustrate the crossover zeros in U^3 and U^{-1}. We show U^{-3} with 180° phase, because that is the result of the fits, within errors. Not shown is $N^{-1}=N^3/\sqrt{3}$, or $N^{-3}=\sqrt{3}N^{-1}$; the amplitude relationships are such that N^3 and N^{-3} cannot be separated and we have plotted $N^3=\sqrt{\sigma_N}$.

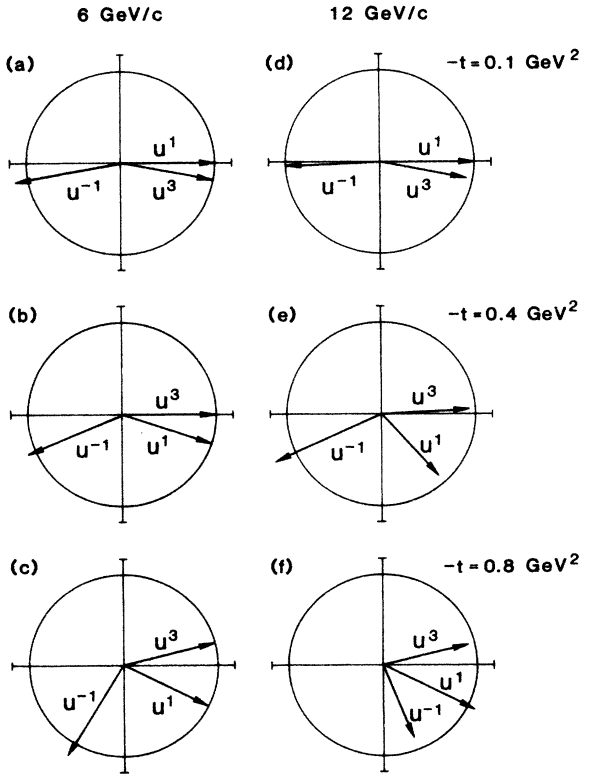

FIG. 26. The orientation in the complex plane of the UP amplitudes U^1_{-+}, U^3_{-+}, and U^{-1}_{-+} for $-t=0.1$ (a) (d), 0.4 (b) (e), and 0.8 GeV^2 (c) (f); (a), (b), (c) refer to 6 GeV/c, and (d), (e), (f) to 11.75 GeV/c, and all amplitudes are in the s channel. The unit circles indicate the expected lengths of the amplitude vectors; we have divided the U^M_{-+} amplitudes by the values which would be consistent with the AQM relations for σ_+, σ_-, and σ_0.

patterns which we have shown above in σ_+, σ_-, and σ_0.

The relative orientations in the complex plane of the important s-channel UP amplitudes, U^3, U^1, and U^{-1} are shown in Fig. 26 for three t values beyond the crossover at $-t=m_\pi{}^2$. In the fits we allowed the phases of the four U^M amplitudes to float, but fixed the s- and p-wave amplitudes by the WM parametrization; this provides a phase reference, although probably only the relative phases in Fig. 26 are significant, since the s and p amplitudes are small and model dependent. The lengths of the amplitude vectors in Fig. 26 are scaled by the AQM values, that is, the values which are consistent with σ_- and σ_0 extracted from Eq. (29); the magnitudes of the U^M amplitudes are within $\sim 15\%$ of the AQM projections. The amplitudes display the approximate phase behavior anticipated above, namely, U^3 and U^{-1} are approximately antiparallel, and U^1 rotates clockwise with respect to U^3, for increasing $-t$. For $-t \simeq 0.25$ GeV^2, U^1 and U^3 cross each other in phase, and this is reflected in the sign change of U_{3-1} [Fig. 24(c) and Eq. (39d)].

A more elaborate amplitude analysis is not warranted, in view of the many model-dependent assumptions that would be needed. However, the results suggest that the main deviations from the WM can be ascribed to (a) NP ρ- and A_2-exchange amplitudes which account for the energy dependence of σ_+ but play a minor role in the polarization, and (b) UP B-exchange contributions which are expected in the AQM and which give rise to large polarization effects by rotating the phase of U^1 relative to U^3 cross section approaches $\sim 50\%$ of the total Δ-production rate for large t ($-t \gtrsim 0.5$ GeV^2). Very similar behavior is seen in $\pi^- p \to \rho^0 n$ and $K^+ n \to K^{*0} p$. The total UP differential cross section, $\sigma_- + \sigma_0$, has t dependence ($e^{\sim 13t}$) and shrinkage ($\alpha_{\text{eff}} \sim t$) as expected for a pion-exchange-dominated reaction. The behavior of σ_-, ρ_{31}, and ρ_{s-1} requires crossover zeros at $-t \approx m_\pi{}^2$ in the $n=0$ double-flip s-channel amplitudes, as expected in the WM. Again, there are strong similarities with the UP production amplitudes in $\pi^- p \to \rho^0 n$ and $K^+ n \to K^{*0} p$.

The comparison of longitudinal and transverse asymmetries leads to an important conclusion: namely, that the NP contributions to the polarizations are small; the polarizations are dominated by UP terms. This is as expected in the simple AQM, where there would be only one independent NP amplitude ($N^3 = \sqrt{3} N^{-1}$) and two UP amplitudes (U^1 and $U^3 \simeq -\sqrt{3} U^{-1}$). Our amplitude analysis allowed for deviations from this simple picture; small N^{-3} and N^1 amplitudes give rise to $\sigma_N A_N / \sigma_N \sim -20\%$ at large $-t$ for the NP cross section. The solution for the UP amplitudes turns out to be qualitatively consistent with the expectations of the AQM, based on input from ρ-ω interference measurements.[7] The large UP spin correlations are explained by interference of π and B exchange, and in the s channel this results in U^1 being out of phase with U^3 and U^{-1}, in the sense predicted by the AQM.

We conclude that the phases and energy dependences of the Δ^{++}-production amplitudes can be described qualita-

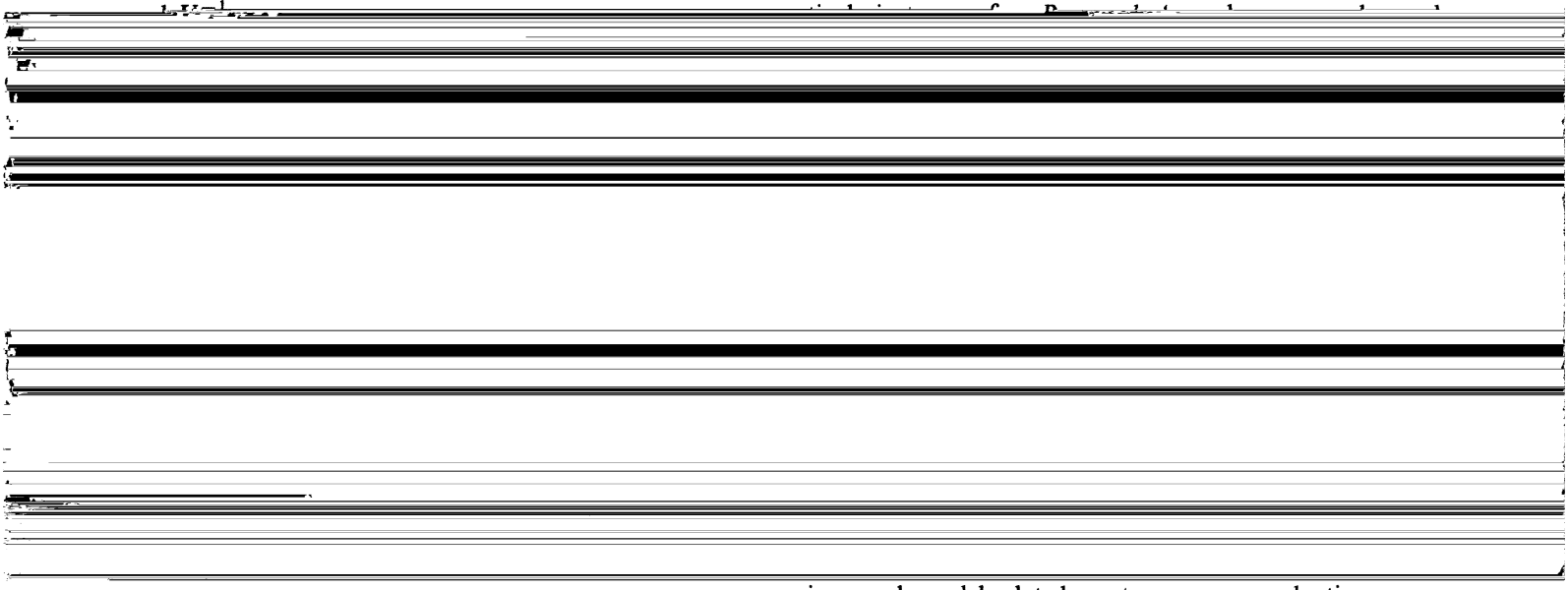

VI. SUMMARY

We have presented DME's and spin correlations for $p_\uparrow p \to p\pi^+ n$ at 3, 4, 6, and 11.75 GeV/c, together with the formalism necessary to interpret the results. The mass and t dependence of the unpolarized DME's can be described adequately by a seven-parameter pion-exchange fit based on the Williams model. This parametrization also describes the off-shell $\pi^+ p$ elastic-scattering contributions to the spin observables, at least for the s-Δ interference terms, which are the most easily isolated. Using this parametrization to predict the analogous contributions from p-Δ interference, we conclude that the spin correlations due to Δ production alone (e.g., Δ-Δ interference terms) are substantial; the overall production asymmetry in quark-model-related vector-meson production reactions. Extrapolated to lower energies, this description would provide a known "background" with which to search for dibaryon effects, which are expected to couple strongly to the ΔN channel. We defer this discussion to another paper.[5]

ACKNOWLEDGMENTS

We acknowledge the technical assistance of I. Ambats, J. Dawson, L. Filips, and E. Walschon. We acknowledge the participation of D. Cohen in the experimental data taking. We thank R. Ely, C. Klindworth, R. Rivetna, and S. Watson for help with the on-line computers and off-line processing, and the ZGS staff for the smooth operation of the accelerator. We acknowledge the original contributions of R. D. Field to the quark-model analysis

where $j=\frac{1}{2}^{\pm},\frac{3}{2}^{+}$ and $l=0,1$ refer to total J and orbital momentum for the $p\pi^+$ system; $q_{p\pi^+}$ is the proton momentum in the $p\pi^+$ RF; and δ_{jl} are the π^+p elastic phase shifts. The relations between s- and t-channel amplitudes are given by the crossing matrix

$$P_{\xi}^{MM'}(t)=d^{j}_{M'/2,M/2}(\chi_\Delta)\cos\frac{\chi_p}{2}$$
$$+\xi(-1)^{l+j+M'/2}d^{j}_{-M'/2,M/2}(\chi_\Delta)\sin\frac{\chi_p}{2} \quad \text{(A2)}$$

at the beam-Δ^{++} vertex, and by the crossing factors

$$r_{++}(t)\approx\left[\frac{t_{\min}}{t}\right]^{1/2}, \quad \text{(A3a)}$$

$$r_{-+}(t)\approx\left[\frac{t-t_{\min}}{t}\right]^{1/2} \quad \text{(A3b)}$$

at the recoil vertex. The angles χ_p and χ_Δ in Eq. (A2) are the crossing angles defined in Sec. III; these angles depend on $M_{p\pi^+}$, and as a result the amplitudes u^M and n^M in Eq. (A1) have some explicit mass dependence.

In the Chew-Low model,[16] with no absorptive effects, we would have

$$u^{1}_{++}(t\text{ channel})=G\frac{\sqrt{-t}}{-t+\mu^2}e^{B(t-t_{\min})}, \quad \text{(A4a)}$$

where

$$G=\left[\frac{G_{\pi NN}{}^2}{2M_N{}^2}\right]^{1/2}e^{B(t_{\min}-\mu^2)}, \quad \text{(A4b)}$$

with all other t-channel amplitudes vanishing; here $\mu^2=m_\pi{}^2$, B is an empirical collimation factor, and

$$[(G_{\pi NN})^2/2\pi M_N{}^2]^{1/2}\simeq 3.6\text{ mb}^{1/2}.$$

The s-channel Born-term amplitudes would then take the form

$$u^{M}_{++}(s\text{ channel})=r_{++}(t)P_{-}^{M1}(t)u^{1}_{++}(t\text{ channel}), \quad \text{(A5a)}$$

$$u^{M}_{-+}(s\text{ channel})=r_{-+}(t)P_{-}^{M1}(t)u^{1}_{++}(t\text{ channel}), \quad \text{(A5b)}$$

with $n^{M}_{++}=0$ and $n^{M}_{-+}=0$. The WM amounts to a recipe for adding absorptive cut contributions to the Born terms. The cuts are most significant in the $n=0$ double-flip amplitudes, which vanish at $t=t_{\min}$ in the Born approximation, but in the WM take on the values

$$u^{3}_{-+}(t'=0)=-n^{3}_{-+}(t'=0)=-\tfrac{1}{2}\tilde{P}^{31}_{-}GS=C^3, \quad \text{(A6a)}$$

$$u^{-1}_{-+}(t'=0)=n^{-1}_{-+}(t'=0)=-\tfrac{1}{2}\tilde{P}^{-11}_{-}GS=C^{-1}, \quad \text{(A6b)}$$

where

$$\tilde{P}_{\xi}^{MM'}=\lim_{(t'\to 0)}\frac{P_{\xi}^{MM'}(t)}{(-t')^{|M-M'|/4}} \quad \text{(A7)}$$

and S is a scale factor ($S=1$ in the WM). As in Ref. 7, we have assigned an empirical t dependence to the t-channel $n=0$ cut contributions away from $t=t_{\min}$. This amounts to writing the s-channel WM cut contributions as

$$u^{M}_{-+}(s\text{-channel cut})$$
$$=[P_{-}^{M3}(t)C^3+P_{-}^{M-1}(t)C^{-1}]e^{B_-t'+D_-t'^2}, \quad \text{(A8a)}$$

$$n^{M}_{-+}(s\text{-channel cut})$$
$$=[-P_{+}^{M3}(t)C^3+P_{+}^{M-1}(t)C^{-1}]e^{B_+t'+D_+t'^2}. \quad \text{(A8b)}$$

The cut contributions of Eq. (A8) are added to the Chew-Low s-channel amplitudes of Eq. (A5). This leaves seven parameters to be determined: G, S, B, B_-, B_+, D_-, and D_+.

The s-channel double-flip amplitudes in this parametrization have the crossover-zero structure which is expected for the WM. Adding Eqs. (A8) and (A5), and taking $S=1$, $B_\pm=B$, and $D_\pm=0$, we have

$$u^{3}_{-+}(s\text{ channel})\approx-\left[\frac{t+\mu^2}{-t+\mu^2}\right]\frac{\tilde{P}^{31}_{-}}{2}Ge^{Bt}, \quad \text{(A9a)}$$

$$u^{-1}_{-+}(s\text{ channel})\approx-\left[\frac{t+\mu^2}{-t+\mu^2}\right]\frac{\tilde{P}^{-11}_{-}}{2}Ge^{Bt}, \quad \text{(A9b)}$$

$$n^{3}_{-+}(s\text{ channel})\approx\frac{\tilde{P}^{31}_{-}}{2}Ge^{Bt}, \quad \text{(A9c)}$$

$$n^{-1}_{-+}(s\text{ channel})\approx-\frac{\tilde{P}^{-11}_{-}}{2}Ge^{Bt}, \quad \text{(A9d)}$$

for small t in the high-energy limit, where $t_{\min}=0$. The n^M amplitudes are smooth in t, whereas the $u^{3,-1}$ amplitudes have zeros at $t=-\mu^2$ in the s channel. Numerically, for the Δ waves, $\tilde{P}^{31}_{-}\approx+3.5$ GeV$^{-1/2}$ and $\tilde{P}^{-11}_{-}\approx-2.7$ GeV$^{-1/2}$, so that u^{3}_{-+}, u^{-1}_{-+}, n^{3}_{-+}, and n^{-1}_{-+} have 180°, 0°, 0°, and 0° phases at $t'=0$, respectively.

The fitted values of the seven parameters are listed in Table I together with the calculated values of $\tilde{P}^{M1}_{-}$. The scale parameters S are close to unity, consistent with the WM. The coupling strengths G should approach the value $3.6e^{B(t_{\min}-\mu^2)}$ [cf. Eq. (A4b)], and this is a fair approximation for higher p_{lab}. The slopes B increase with p_{lab} as expected for Regge shrinkage. The slopes $B_\pm$ are significantly larger than B; presumably $B_\pm$ and $D_\pm$ help to mock up the effects of non-pion-exchange contributions.

*Present address: Physics Department, University of Arizona, Tucson, AZ 85721.

†Present address: AT&T Information Systems, Denver, CO 80234.

[1]A. B. Wicklund, in *High Energy Physics with Polarized Beams and Targets*, proceedings of the Argonne Symposium, 1976, edited by M. L. Marshak (AIP Conf. Proc. No. 35) (AIP, New York, 1976).

[2]F. Shimizu *et al.*, Nucl. Phys. **A386**, 571 (1982), (0.9—2.0 GeV/c); W. J. Fickinger, E. Pickup, D. K. Robinson, and E. O. Salant, Phys. Rev. **125**, 2082 (1962), (2.8 GeV/c); G. Alexander *et al.*, *ibid.* **154**, 1284 (1967), (5.5 GeV/c); J. D.

Mountz *et al.*, Phys. Rev. D **12**, 1211 (1975), (6.0 GeV/c); E. Colton *et al.*, Phys. Rev. Lett. **23**, 342 (1969), (6.6 GeV/c); G. Alexander *et al.*, Phys. Rev. **173**, 1322 (1968), (6.92 GeV/c); J. Ginestet, D. Manesse, T. H. Anh, and D. Vignaud, Nucl. Phys. **B13**, 283 (1969), (8.1 GeV/c); S. P. Almeida *et al.*, Phys. Rev. **174**, 1638 (1968), (10.0 GeV/c); Z. M. Ma, G. A. Smith, R. J. Sprafka, and G. T. Williamson, Phys. Rev. Lett. **24**, 1031 (1970), (13.0, 18.1, 21.1, 24.2 GeV/c); Y. Gnat *et al.* Nucl. Phys. **B54**, 333 (1973), (16.2 GeV/c); H. Boggild *et al.*, Phys. Lett. **30B**, 369 (1969), (19.0 GeV/c); W. E. Ellis *et al.*, Phys. Rev. Lett. **21**, 697 (1968), (28.5 GeV/c); N. Kwak *et al.*, Phys. Lett. **62B**, 359 (1976), (280, 510, 1090 GeV/c); H. de Kerret *et al.*, *ibid.* **69B**, 372 (1977), (280, 510, 1090, 1500 GeV/c).

[3]R. L. Eisner *et al.*, Phys. Rev. D **20**, 596 (1979), (6 GeV/c).

[4]H. Becker *et al.*, Nucl. Phys. **B150**, 301 (1979); A. de Lesquen *et al.*, Phys. Rev. D **32**, 21 (1985).

[5]A. B. Wicklund *et al.* (unpublished).

[6]P. K. Williams, Phys. Rev. D **1**, 1312 (1970).

[7]A. B. Wicklund *et al.*, Phys. Rev. D **17**, 1197 (1978).

[8]R. Diebold *et al.*, Phys. Rev. Lett. **31**, 904 (1974).

[9]A. J. Pawlicki *et al.*, Phys. Rev. D **15**, 3196 (1977).

[10]R. Diebold *et al.*, Phys. Rev. Lett. **35**, 632 (1975).

[11]S. L. Kramer *et al.*, Phys. Rev. D **17**, 1709 (1978).

[12]M. W. Arenton *et al.*, Phys. Rev. D **25**, 22 (1982).

[13]H. Hinterberger *et al.*, Rev. Sci. Instrum. **41**, 413 (1970).

[14]H. A. Neal and M. J. Longo, Phys. Rev. **161**, 1374 (1967); G. Cozzika *et al.*, *ibid.* **164**, 1672 (1967); M. G. Albrow *et al.*, Nucl. Phys. **B23**, 445 (1970); M. Borghini *et al.*, Phys. Lett. **31B**, 405 (1970); **36B**, 501 (1971); J. H. Parry *et al.*, Phys. Rev. D **8**, 45 (1973); A. Lin *et al.*, Phys. Lett. **74B**, 273 (1978); D. Miller *et al.*, Phys. Rev. Lett. **36**, 763 (1976); Phys. Rev. D **16**, 2016 (1977); K. Abe *et al.*, Phys. Lett. **63B**, 239 (1976).

[15]H. Spinka *et al.*, Nucl. Instrum. Methods **211**, 239 (1983).

[16]G. C. Chew and F. E. Low, Phys. Rev. **113**, 1640 (1959); E. Ferrari and F. Selleri, Nuovo Cimento Suppl. **24**, 453 (1962).

[17]A. B. Wicklund, Argonne Report No. ANL-HEP-TR-86-21, 1986 (unpublished).

[18]A. Bialas, A. Kotanski, and K. Zalewski, Nucl. Phys. **B78**, 1 (1971); A. Bialas and K. Zalewski, *ibid.* **B6**, 449 (1968); **B6**, 465 (1968); **B6**, 478 (1968); **B6**, 483 (1968); L. Stodolsky and J. J. Sakurai, Phys. Rev. Lett. **11**, 90 (1963); G. C. Fox, in *Phenomenology in Particle Physics, 1971,* proceedings of the Conference, Caltech, 1971, edited by C. B. Chiu, G. C. Fox, and A. J. G. Hey (Caltech, Pasadena, 1971); R. D. Field in *Proceedings of the XVII International Conference on High Energy Physics, London, 1974,* edited by J. R. Smith (Rutherford Laboratory, Chilton, Didcot, Berkshire, England, 1974); A. Itano *et al.*, in *High Energy Physics with Polarized Beams and Polarized Targets,* proceedings of the 1980 International Symposium, Lausanne, Switzerland, edited by C. Joseph and J. Soffer, Experientia Supplementum Vol. 38 (Birkhäuser, Basel, Switzerland, 1981).

[19]A. de Lesquen *et al.* Saclay Report No. DPhPE 82-01, 1982 (unpublished); also F. Lehar and M. Svec (private communication).

[20]K. J. M. Moriarty and H. Navelet, Phys. Lett. **71B**, 208 (1972).

[21]We used the polynomial parametrizations of the data as input, rather than the raw data points, in order to obtain a continuous solution which did not show systematic deviations from the measured DME's; the polynomials describe the data adequately, and the amplitude fits agreed with the polynomials within $\sim \pm 0.01$ on any of the Δ-Δ spin correlations.